Reduction of SynGAP-γ, disrupted splicing of *Agap3*, and oligodendrocyte deficits in *Srrm2* mice, a genetic model of schizophrenia and neurodevelopmental disorder

Sameer Aryal,[1,4,*] Chuhan Geng,[1] Min Jee Kwon,[1] Zohreh Farsi,[1] Nathaniel Goble,[1] Ahmet S. Asan,[1] Kira Brenner,[1] Nate Shepard,[1] Olivia Seidel,[2] Yining Wang,[1] Ally Nicolella,[1] Bryan J. Song,[1] Hasmik Keshishian,[2] Steven A. Carr,[2] Jen Q. Pan,[1] Morgan Sheng[1,3,*]

1. Stanley Center for Psychiatric Research, Broad Institute of MIT and Harvard, Cambridge, MA 02142, USA
2. The Proteomics Platform, Broad Institute of MIT and Harvard, Cambridge, MA 02142, USA
3. Department of Brain and Cognitive Sciences, Massachusetts Institute of Technology, Cambridge, MA 02142, USA
4. Lead contact

*Correspondence: msheng@broadinstitute.org (M.S.), saryal@broadinstitute.org (S.A.)

Abstract

Rare loss-of-function (LoF) variants in *SRRM2*, which encodes the SRRM2 splicing factor, are associated with schizophrenia and a neurodevelopmental disorder. How haploinsufficiency of *SRRM2* leads to brain dysfunction is unknown. We find that *Srrm2*$^{+/-}$ mice display (i) large-scale changes in gene expression in neuronal and glial cells, affecting synapse-related and other common molecular pathways across multiple brain regions, (ii) reduction of multiple key postsynaptic proteins, including the gamma isoform of SynGAP, itself encoded by a neurodevelopmental disorder risk gene, (iii) abnormal splicing and elevated expression of Agap3, a SynGAP interactor, (iv) reduced numbers of oligodendrocytes accompanied by decreased expression of myelin-related mRNAs and proteins, and (v) behavioral and EEG abnormalities, including reduction in sleep spindles that phenocopy humans with schizophrenia. Our findings provide insights into the molecular and neurobiological mechanisms of and potential therapeutic avenues for schizophrenia and the *SRRM2* LoF neurodevelopmental disorder.

Introduction

Schizophrenia (SCZ) is a common psychiatric disorder and a leading cause of disability in young adults (1). Large-scale exome- and targeted-sequencing studies of humans with SCZ have associated rare heterozygous protein-truncating variants in serine/arginine repetitive matrix 2 (*SRRM2*) with substantially elevated disease risk (odds ratio=9.12; combined *P*-value = 7.2×10^{-7})(2, 3). Exome sequencing of ~31000 parent/offspring trios has also linked heterozygous LoF of *SRRM2* to a syndromic neurodevelopmental disorder that presents with mild intellectual disability (ID) and mild-to-moderate developmental delay (DD), most prominently in language acquisition (4, 5).

A gene highly intolerant to LoF mutations (probability of LoF intolerance = 1)(5), *SRRM2* encodes a ~300 kDa RNA-binding protein that is thought to regulate pre-mRNA splicing (6–8). In yeast, the ortholog of Srrm2 co-purifies with spliceosome components (9). In mammalian cells, Srrm2 primarily localizes to and acts as a core scaffold of nuclear speckles (8, 10), which are irregularly shaped biomolecular condensates thought to regulate pre-mRNA splicing by acting as reservoirs of small nuclear ribonucleoprotein particles (snRNPs), splicing factors, and spliceosome subunits (11).

SCZ's genetic link to *SRRM2*—and consequently to speckles and mRNA splicing—is particularly notable because (i) large-scale transcriptomic analysis of humans with SCZ has revealed an outsized impact on mRNA isoform and splicing regulation in the brains of individuals with SCZ, compared to those with bipolar disorder or autism (12), and (ii) in the human fetal cortex, genomic regions in proximity of nuclear speckles are enriched for SCZ common variant risk loci (13). These findings, together with the human genetics association, support a mechanistic relationship between *SRRM2*, nuclear speckles, and SCZ pathophysiology.

Little is known about the pathomechanisms of SCZ or the *SRRM2* LoF disorder. We reasoned that a comprehensive characterization of *Srrm2* heterozygous mutant mice—at transcriptomic, proteomic, neurophysiological, and behavioral levels—should provide insight into what goes wrong in the brain of this genetic animal model of SCZ and *SRRM2* LoF disorder. In this study, we performed bulk and single-nucleus RNA sequencing of multiple brain regions at different ages, synapse proteomics of the neocortex, and behavioral and electroencephalogram (EEG) analyses to uncover the endophenotypes of *Srrm2* heterozygous LoF mice.

Combined, we find that haploinsufficiency of *Srrm2* in mice leads to impaired expression of synaptic genes and key postsynaptic proteins, deficits in oligodendrocytes and myelination, and EEG changes that resemble those seen in humans with SCZ. By uncovering molecular and neurobiological alterations resulting from the disruption of *Srrm2*, our study provides insights into disease mechanisms of SCZ and the *SRRM2* LoF neurodevelopmental disorder.

Results

Large-scale and correlated transcriptomic changes across different brain regions in *Srrm2*$^{+/-}$ mice

We studied a previously generated *Srrm2* mutant that harbors a deletion of exon 9 in the *Srrm2* locus (14), which we confirmed by Sanger sequencing (Fig. S1A) and PCR (Fig. S1B). While heterozygous mutants of this mouse line are generally healthy, homozygous knockouts show complete penetrance of preweaning lethality (14); so we focused our investigations on the heterozygous (+/-) genotype, which is also the genotype linked to elevated risk of SCZ and the *SRRM2* LoF syndrome.

To evaluate the impact of *Srrm2* LoF on the brain in an unbiased manner, we used RNA sequencing to profile gene expression changes (compared to wild-type (WT) littermates) in 8 brain regions of *Srrm2* heterozygous mutant mice (henceforth *Srrm2*$^{+/-}$) at 1- and 3-months of age (Fig. S1C). Principal component analysis showed clear clustering of bulk RNA-seq samples by brain region, consistent with accurate tissue dissection (Fig. S1C). The *Srrm2* gene itself was highly expressed across brain regions in WT animals (Fig. S1D), most prominently in the prefrontal cortex (PFC) and thalamus (TH), and was reduced in *Srrm2*$^{+/-}$ mice—across the entire coding sequence (Fig. S1E)—to less than 50% of WT in most brain regions (Fig. S1D).

Differential expression (DE) analysis of bulk-RNA-seq data revealed that gene expression was strongly affected in all brain regions in *Srrm2*$^{+/-}$ mice. At 1-month of age, *Srrm2*$^{+/-}$ brains showed hundreds to thousands of DE genes (DEGs; defined as genes with FDR-adjusted $P < 0.05$ in DE analysis) in diverse brain regions, with the striatum (ST), substantia nigra (SN), and cerebellar cortex (CC) having the largest number of DEGs (Fig. 1A).

For every brain region there were many more DEGs at 1-month than at 3-months of age in *Srrm2*$^{+/-}$ mice (Fig. 1A; Table S1).

By comparing log2 fold change (Log2FC) of all individual genes between different brain regions, we observed considerable similarity in transcriptomic changes across brain regions, particularly in 1-month old *Srrm2*$^{+/-}$ mice (Pearson's r = 0.20–0.63, median r = 0.39, $P < 2x10^{-16}$ in every comparison; Fig. 1B). Restricting this comparison to only the 6429 DEGs (FDR < 0.05 in at least one brain region) revealed even stronger correlations between different brain regions (Fig. 1C; r = 0.35–0.76, median r = 0.55).

Correspondingly, DEGs showed remarkable overlap between different brain regions (Fig. S1F). The 28 DEGs shared across all regions (Fig. S1G), and the 1299 DEGs shared between any two regions (Fig. S1H), showed consistent directional changes across brain regions. Evaluation of the log2FCs in ST against those in PFC—two brain regions with substantially different cell type populations—also showed concordant changes (r = 0.40 for all genes, r = 0.54 for DEGs in either PFC or ST; r = 0.88 for genes DE in both PFC and ST; Fig. 1D). Of note, *Nptx2* (neuronal pentraxin 2, an activity regulated gene) was downregulated in both ST and PFC bulk RNA-seq (Fig. 1D); the NPTX2 protein has been reported to be reduced in the cerebrospinal fluid (15) and PFC synaptic fractions (16) of humans with SCZ.

Among DEGs shared across at least four brain regions of 1-month-old *Srrm2*$^{+/-}$ mice (n=488; Table S1), we noted widespread reduction in *Grin1* (NMDA receptor constitutive subunit), *Rab26* (synaptic vesicle autophagy regulator), and *Gpt* (alanine aminotransferase, which metabolizes alanine to produce glutamate (Fig. 1E). *Fmr1*, *Pten*, *Taok1* (all DD/ID associated genes), and *Gpr34* (microglia homeostasis regulator) were elevated across many regions (see Fig. 1E, which also shows other interesting DEGs with their functions annotated).

At 3 months, there were similar, albeit more modest, correlations in gene expression changes and overlap in DEGs across brain regions of *Srrm2*$^{+/-}$ mice (Fig. S1I–K). The 26 genes differentially expressed in four or more brain regions in 3-month-old *Srrm2*$^{+/-}$ mice also exhibited largely consistent changes across different brain regions (Fig. S1L). Gene expression changes at 1-month vs 3-month were also correlated in all brain regions (Pearson's r = 0.14 (HP)–0.58 (PFC) transcriptome-wide, r = 0.15 (HP)–0.70 (PFC) for DEGs at either age; $P < 2x10^{-16}$ in all comparisons) except in ST, which had limited correlation (r = -0.008 transcriptome-wide, r = 0.025 for DEGs at either age).

To gain insight into the molecular pathways that were perturbed with *Srrm2* LoF, we performed gene set enrichment analysis (GSEA) on the bulk RNA-Seq data from all brain regions using mSigDb (17), and SynGO (18) gene ontology (GO) terms, focusing on 1-month age, when transcriptomic changes were greater (Fig. 1A). Consistent with the transcriptome-wide correlations in gene expression changes, we observed multiple GO terms in mSigDB that were commonly changed across most brain regions in 1-month-old *Srrm2*$^{+/-}$ mice. Gene sets related to synapse/glutamatergic synapse, ribosomes/translation, mitochondria/respiration, and myelination (a gene set of particular interest, see below) were downregulated, while those related to DNA binding and transcription regulation were upregulated (Fig. 1F; Table S2).

Using SynGO annotated terms (Fig. 1G), we observed downregulation of both presynapse- and postsynapse-related gene sets in all brain regions of 1-month-old *Srrm2*$^{+/-}$ mice, except SSC, which showed modest upregulation of many synapse-related terms (Fig.

1G). GSEA using SynGO and mSigDb genesets both highlighted downregulation of synaptic translation-related genes across all brain regions, especially the cerebellum (Fig. 1F, 1G).

Genes associated with bipolar disorder (19) and schizophrenia (20) by GWAS (or by SCHEMA (2)) were enriched in the downregulated genes in most of the brain regions of *Srrm2*$^{+/-}$ mice, especially the thalamus (Fig. 1G). Meanwhile, ASD risk genes from the SFARI database were enriched in upregulated genes in most brain regions. Only in the thalamus was there concordant enrichment of ASD and SCZ and BP genes in downregulated genes (Fig. 1G).

Activity regulated genes—the expression of which can be used as a surrogate measure of neuronal activity—were enriched in downregulated genes in PFC and ST, and in upregulated genes in HP, SSC, SN (Fig. 1G), indicating differential effects on regional brain activity in *Srrm2* mutants.

Because elevated dopamine signaling in the striatum (ST) is implicated in the pathophysiology of SCZ (21), we were intrigued to find by GSEA that the "response to dopamine" gene set (mSigDB) was significantly upregulated at 1 month age specifically in the striatum of *Srrm2*$^{+/-}$ mice (Fig. 1F). Closer inspection revealed that although most genes in this gene set tended to increase (in line with the GSEA result), some genes were reduced in expression (Fig. 1H). Interestingly, the genes that were robustly increased in *Srrm2*$^{+/-}$ striatum—including *Htr2c, Drd1*, and *Drd2* which encode the serotonin 2C- and dopamine D1- and D2-receptors, and other genes like *Adcy5*, *Rgs9*, *Rgs8*, *Nsg2*, *Gnal* (Fig. 1H)—are known to be highly enriched in spiny projection neurons (SPNs) of the striatum (22). In contrast, the genes in the "response to dopamine" set that were robustly reduced (*Adcy6*, *Gnas*, *Htr1a*, *Htr5a*) are selectively expressed in other cell types (such as inhibitory interneurons) of the striatum (Fig. 1H)(22). These data are suggestive of a major perturbation of the striatal circuitry in *Srrm2*$^{+/-}$ mice.

Srrm2 LoF causes isoform-specific changes in SynGAP and Agap3 at the synapse

The transcriptomics GSEAs indicated widespread changes in synapse-related pathways across all brain regions in *Srrm2*$^{+/-}$ mice. To investigate synaptic changes at the protein and proteoform level we performed mass spectrometry-based quantitative proteomics on synapse fractions purified from cerebral cortex of 1- and 4 month-old *Srrm2*$^{+/-}$ mice.

We observed 35 and 44 differentially expressed proteins (DEPs; defined as *P*-value < 0.01) in 1- and 4-month-old *Srrm2*$^{+/-}$ mice synapses, respectively (Fig. 2A, 2B; Table S2). GSEA of the synaptic proteome changes using SynGO gene sets indicated a prominent reduction of several protein sets related to post-synaptic structure and function in 4-month-old *Srrm2*$^{+/-}$ mice (Fig. 2C, Table S2). We noted reductions in glutamatergic signaling proteins, especially GTPase regulatory proteins, such as SynGAP (encoded by *Syngap1*) and its binding partners Iqsec2, Iqsec1 (23); the retrovirus-like activity-dependent intercellular signaling protein Arc; multiple glutamate receptor subunits and associated proteins (Gria3, Gria2, Olfm2, Grid2ip); and postsynaptic scaffolding and cytoskeletal anchoring proteins (Anks1b, Psd95 (encoded by *Dlg4*), Cript)(Fig. 2D, Fig. S2A). This downregulation of key postsynaptic proteins—reminiscent of synapse proteome changes in humans with SCZ (16)—was not observed in 1-month-old *Srrm2*$^{+/-}$ synapses (Fig. S2B, Fig. 2C), indicating that these major postsynaptic protein changes are delayed relative to the transcriptomic changes in synapse pathways (Fig. 1F, 1G). Additionally, GSEA with mSigDB terms showed that protein sets related to RBPs, ribosomes, and translation were upregulated in the synapses of 4-month-old *Srrm2*$^{+/-}$ mice; these same pathways were either downregulated or minimally changed at 1-month (Fig. 2C, Fig. S2C)

further highlighting that *Srrm2* LoF remodels the synapse proteome in an age-dependent manner (Table S2).

Among all DEPs, a SynGAP proteoform showed the largest drop in protein level (reduced by ~70%) and the most significant reduction (by *P*-value) in *Srrm2*$^{+/-}$ synapse fractions at both 1- and 4-months of age (Fig. 2A, 2B). This finding is especially interesting because *Syngap1* haploinsufficiency is a common cause of DD, as well as of ID and autism, all of which are observed in humans with *SRRM2* LoF mutations (5, 24). Given the large reduction of SynGAP, it was also striking to find that Agap3—a known interactor of SynGAP (21–23)—was among the two most upregulated proteins (elevated ~60%) in *Srrm2*$^{+/-}$ synapses at both ages (Fig. 2A, 2B).

SynGAP exists in four isoforms (α1, α2, β, and γ) due to alternative splicing of the 3' terminus of *Syngap1* (Fig. S2D) (25, 26), while two isoforms of Agap3 have been described—full length (Agap3-FL) and an N-terminally truncated isoform, called Crag (Fig. S2E) (27). Detailed analysis of MS/MS spectra of peptides revealed that in *Srrm2*$^{+/-}$ synapses at both ages, it was specifically the gamma isoform of SynGAP (SynGAP-γ) that was diminished, and specifically the Agap3-FL isoform that was increased (Fig. 2E).

By western blotting of cortical synaptic fractions from an independent cohort of *Srrm2*$^{+/-}$ mice, we confirmed the changes in Agap3 and SynGAP isoforms, as well as in two other proteins (Gpt and Pak4) that changed in an age-specific manner (Fig. 2F, 2G). The increase in Agap3-FL and reduction in SynGAP-γ was also seen at 1 year of age, indicating that this biochemical phenotype persists into late adulthood in *Srrm2*$^{+/-}$ mice.

Altered *Agap3* mRNA splicing across the brain of *Srrm2*$^{+/-}$ mice

There were no major changes in *Agap3* and *Syngap1* mRNA expression as measured by standard gene-level RNA seq analysis (Fig. S3A). However, isoform-specific alterations may be masked when considered in aggregate. We therefore investigated mRNA isoform abundance changes genome-wide by meta-analyzing *P*-values of changes of all isoforms of a given gene (derived from differential isoform expression analysis) to obtain a gene-level *P*-value for every gene (see Methods and ref. (28)). Using this approach, we observed *Agap3* to be among the most significant DEGs across all brain regions at both 1- and 3-month-old *Srrm2*$^{+/-}$ mice (Fig. 3A; Table S3). Of the six annotated mRNA isoforms of *Agap3* (*201* through *206*), most were changed with low *P*-values in every brain region at both ages (Fig. S3B), and the aggregation of the *P*-values of the individual isoforms resulted in highly significant *P*-values for the *Agap3* gene (Fig. 3A).

Among the individual mRNA isoforms of *Agap3*, those that encompassed the 3' end of *Agap3* were upregulated in the brains of *Srrm2*$^{+/-}$ mice (by ~60% for *Agap3-201,* which encodes the canonical Agap3-FL; Fig. 3B–D). Conversely, isoforms that lacked exons towards the 3' end (including *Agap3-206*, annotated as encoding Crag) were downregulated (Fig. 3B–D). These findings suggested that *Agap3* splicing may be altered with *Srrm2* LoF. Indeed, annotation-free examination of local splicing changes revealed that a singular intron cluster of *Agap3* (among 6 clusters) was prominently differentially spliced in every brain region of 1-month-old and ⅞ regions of 3-month-old *Srrm2*$^{+/-}$ mice (Fig. 3E; Table S3), with the complex splicing alteration leading to increased skipping of exon 9, the terminal exon of Crag that also harbors its stop codon (Fig. 3F).

These findings demonstrate that *Srrm2* LoF favors splicing of *Agap3* towards increased production of its full-length mRNA isoform (which encodes Agap3-FL). Consistent with this mechanism, Agap3-FL protein was markedly elevated (~60-95%) in P2 fractions (see Methods) of the cerebellum, hippocampus, and striatum, as well as in total extracts of the cortex and hippocampus (Fig. 3G, 3H, Fig. S3C).

In contrast to *Agap3*, *Syngap1* was notably unchanged in *Srrm2*$^{+/-}$ mice in terms of mRNA splicing and isoform expression (Fig. 3A, 3E). Nonetheless, western blot examination of the same P2 fractions for SynGAP-γ protein—SynGAP-γ is not readily detectable in total brain extracts—revealed ~60-70% reduction of SynGAP-γ in *Srrm2*$^{+/-}$ hippocampus and striatum (Fig. 3G, 3H, Fig. S3C; SynGAP-γ was not detected in cerebellum).

Western blots of Agap3 and SynGAP1-γ in individual animals showed that a large increase in Agap3-FL was associated with a large reduction in SynGAP-γ (Fig. 3H). Comparison of the MS/MS abundances of Agap3-FL against that of SynGAP-γ in the synapse proteomics also revealed a striking negative correlation between these two proteins across many individual mice (Fig. 3I). Based on the known interaction between Agap3 and SynGAP, and the lack of evidence for any transcriptomic or splicing change in *Syngap1*, we hypothesize that the increase in Agap3-FL protein (due to altered splicing) causes the reduction of SynGAP-γ protein at the synapse in *Srrm2* mutant mice.

Reduced oligodendrocyte numbers, and decreased expression of myelin-related mRNAs and proteins in *Srrm2*$^{+/-}$ mice

To examine the impact of *Srrm2* LoF on specific cell types of the brain, we carried out single nucleus RNA-Seq, focusing on the striatum and the prefrontal cortex (PFC) of 1-month-old *Srrm2*$^{+/-}$ mice. Cell types were inferred using UMAP-based unsupervised clustering and annotated based on expression of marker genes (Fig. 4A).

Cell composition analysis revealed a reduction in proportion of oligodendrocytes (ODCs) in both PFC (reduced by ~23%) and striatum (by ~16%) of *Srrm2*$^{+/-}$ mice (Fig. 4B, 4C; Table S4). Accompanying the ODC reduction was a ~11% increase in proportion of astrocytes in the PFC (Fig. 4B). In the striatum, the proportion of inhibitory neurons rose by ~7% (Fig. 4C), driven by ~7-8% elevation in proportion of both direct- and indirect- SPNs (which express D1 and D2 dopamine receptors, respectively) (Fig. S4A), which may explain in part the increase of D1/D2 neuron-specific genes in striatum bulk RNA-seq (Fig. 1H).

There is substantial evidence for decline in ODC numbers and for dysfunction of dopamine systems in humans with SCZ (29, 30). We observed a striking negative correlation between inhibitory neuron and ODC proportions in the striatum across individual WT and *Srrm2*$^{+/-}$ mice (Fig. 4D), suggesting a close relationship between these (otherwise very different) pathophysiological mechanisms in SCZ. Additionally, the observations that (i) ODCs are the only cell type consistently changed in the same direction in both striatum and PFC (Fig. 4B, 4C), and (ii) nearly all *Srrm2*$^{+/-}$ mice have fewer *numbers* of ODCs in the striatum, compared to every WT animal—which is not the case for inhibitory neurons (Fig. S4B)—suggest that the increase in inhibitory neuron proportions in the striatum of *Srrm2*$^{+/-}$ mice may be a consequence of the decline in ODC numbers.

Consistent with the reduction in proportion (and number) of ODCs (Fig. 4B, 4C, Fig. S4B), we observed significant downregulation of the myelin sheath gene set by GSEA of bulk

RNA-Seq of 1-month-old PFC and striatum of *Srrm2*$^{+/-}$ mice (Fig. 1F). In fact, the myelin sheath gene set was downregulated in bulk RNA-Seq of most brain regions at both 1- and 3-months of age in *Srrm2*$^{+/-}$ mice (Fig. 4E, Fig. 1F). Similarly, expression of an ODC-enriched marker gene set (see Methods) was reduced in most brain regions at both ages (Fig. S4C).

Although it is substantially depleted during purification of synapses, myelin is nonetheless present in synapse fractions (31); myelin proteins therefore can be reliably quantified in synapse fractions with sensitive approaches like mass-spectrometry. We noted in our synapse proteomics data that gene/protein sets related to oligodendrocyte differentiation were enriched among downregulated proteins in *Srrm2*$^{+/-}$ synapse fractions (Fig. 2C). Remarkably, about a third (10/27) of downregulated DEPs in 1-month-old *Srrm2*$^{+/-}$ synapse fractions (Fig. S4D) were either exclusively expressed or highly enriched in ODCs (Fig. 4F)(32). Most of the DEPs that are expressed primarily in ODCs (ex. CNPase (encoded by *Cnp*), Mbp, Mag, Bcas1, Opalin, Gjc2) are known to be specific components of the myelin sheath. The same set of ODC/myelin-associated proteins were found also at lower levels than WT in 4-month-old *Srrm2*$^{+/-}$ synapses, including key myelin proteins Plp, CNPase, Mbp, Mag, although the changes did not reach significance for any individual protein (Fig. 4G).

We validated the proteomics findings by western blotting of *total* lysates of cortex, striatum, and hippocampus, which showed ~15-40% reduction of Mbp and CNPase protein levels in these brain regions of 1-month-old *Srrm2*$^{+/-}$ mice, with particularly robust reduction in the striatum (Fig. 4H; Fig. S4E). We also confirmed by western blotting that CNPase was reduced ~25% in synapse fractions purified from the cortex of an independent cohort of 1-month-old *Srrm2*$^{+/-}$ mice (Fig. 4H). Thus, myelin proteins are downregulated in total extracts as well as in synaptic fractions of *Srrm2*$^{+/-}$ mouse brain.

Several lines of evidence therefore suggest that myelination is decreased—correlated with a reduction in ODC numbers—in the brains of *Srrm2*$^{+/-}$ mice. What might cause the decline in ODC numbers? By examining the RNA-Seq datasets for changes in regulators of ODC differentiation, we found that *Qki*, which encodes an RBP that functions as a master regulator of ODC development (33), was among the most prominent DEGs—as measured by aggregation of *P*-values of isoform changes—across all brain regions of 1-month-old *Srrm2*$^{+/-}$ mice (Fig. 4I). *Qki* mRNA isoforms lacking its first exon (*205* and *203*) were downregulated, whereas all other isoforms—including *Qki-201* whose protein product Qki7 is highly enriched in ODCs (34)—were upregulated (Fig. S4F, S4G). Interestingly, *Qki* showed no significant difference at 3-month age (Fig. 4I) when myelin protein reductions in *Srrm2*$^{+/-}$ were more modest (Fig. 4G).

Srrm2 LoF causes pervasive gene expression changes in neuronal and glial cells

By performing DE analysis on the snRNA-seq data, we found that *Srrm2*$^{+/-}$ mice exhibited upwards of ~1000 unique DEGs (defined as genes with FDR-adjusted $P < 0.01$ in DE analysis) aggregated across all cell types in the PFC, and ~500 unique DEGs aggregated across all cell types in the striatum (Fig. 5A; Table S5). Transcriptomic changes were observed in all subtypes of neurons in both regions (Fig. 5A), with the largest number of DEGs seen in excitatory neurons of the PFC (especially layer 2/3 and 6 (L2/3IT and L6IT), and in inhibitory neurons of the striatum (direct- and indirect- SPNs) (Fig. 5A). Non-neuronal cells also showed sizable snRNA-seq changes, most prominently in astrocytes in the PFC and ODCs in the striatum. Thus, losing one copy of *Srrm2* causes extensive and pervasive changes in nuclear RNA expression across neuronal and glial cells in mice.

GSEA of the snRNA-seq changes revealed that synapse- and neuron development-related terms were upregulated in most excitatory neuron-types of the PFC in *Srrm2*$^{+/-}$ mice (Fig. 5B; Table S5). Inhibitory neurons (dSPNs, iSPNs) of the striatum in *Srrm2*$^{+/-}$ mice exhibited upregulation of some specific gene sets related to pre- and post-synaptic structure and function (e.g. presynaptic active zone, postsynaptic membrane), but the wider synapse sets (such as Synapse, Presynapse, Postynapse) were downregulated (Fig. 5B). The latter result in striatal SPNs may be driven by downregulation of postsynaptic endosome and postsynaptic cytoskeleton gene sets, which did not occur in PFC excitatory neurons (Fig. 5B).

In glial cells, several gene sets, including those related to cell-adhesion (*Ctnna3*, *Cdh19*, *Itgad*), focal adhesion assembly (*Ptpra, Fmn1*), sodium ion import (*Slc5a6*, *Slc8a1*, *Slc6a1*), fibrillar collagen (*Col11a2*, *Col27a1*), and chemokine response (*Robo1*, *Stk39*) were upregulated in ODCs, while terms related to bone morphogenetic protein (BMP) receptor activity (*Chrdl1*, *Bmpr1b*) were downregulated in PFC astrocytes (Fig. 5B). Pathways related to sterol/cholesterol biosynthesis—recently reported to be downregulated in postmortem PFC astrocytes of humans with SCZ (35)—were significantly upregulated in astrocytes of PFC but not significantly changed in striatum in *Srrm2*$^{+/-}$ mice.

Expression of the activity-regulated gene set, which can be used as surrogate of neuronal activity, was strongly decreased by GSEA in both direct and indirect SPNs of *Srrm2*$^{+/-}$ mice (Fig. 5B, 5C). Dopamine-induced genes, which overlap somewhat with the activity-regulated gene set, were also downregulated in SPNs (Fig. 5B, 5C). Overall, these snRNA-seq changes suggest that neuronal activity and/or dopamine signaling may be diminished on a per cell basis in *Srrm2*$^{+/-}$ SPNs, the main neuron-type of the striatum. However, we note that the number and proportion of D1 and D2 SPNs went up in striatum (see above, Fig. 4). Interestingly, dopamine-induced genes were upregulated in excitatory neurons of PFC—particularly in L6CT and LCIT neurons—which were unaltered in proportion (Fig. 5B).

Correlated with their reduced expression of activity-regulated genes, striatal SPNs of *Srrm2*$^{+/-}$ mice showed downregulation of certain metabolic pathways (ribosome, protein synthesis, mitochondria, oxidative phosphorylation; Fig. 5B). RNA binding and RNA splicing-related gene sets (including *Son*, whose protein product forms a core scaffold of nuclear speckles with Srrm2), were also downregulated in SPNs (as well as in ODCs) of striatum, but were unchanged in PFC neurons (Fig. 5B).

Behavioral abnormalities in *Srrm2*$^{+/-}$ mice

We evaluated young adult *Srrm2*$^{+/-}$ mice (4-5 months age) and their WT littermates in a battery of behavioral assays. *Srrm2*$^{+/-}$ mutant mice of either sex showed no significant difference from WT in novel object recognition (Fig. S5A, S5B), 3-chamber social interaction (Fig. S5C), preference for novel animals in 3-chamber (Fig. S5D), or Y-maze (Fig. S5E).

Continuous homecage monitoring for 1 month revealed ~15% reduction (P = 0.2) in average locomotor activity (Fig. S5F), especially in the dark cycle, but no obvious change in daily locomotor activity rhythms in *Srrm2*$^{+/-}$ mice (Fig. S5G). Activity on a free-spinning running wheel placed in the home cage was reduced three-fold (Fig. 6A), while in the open field test, *Srrm2*$^{+/-}$ mice showed ~17% reduction in movement (total distance traveled; Fig. 6B, 6C), ~40% reduction in jump counts (Fig. 6D), and ~30% reduction in ratio of center/margin distance traveled (Fig. 6E). Effects observed in the open field test were notably stronger in female *Srrm2*$^{+/-}$ mice compared to male mice (Table S6). In the forced swim test (FST), *Srrm2*$^{+/-}$ mice showed ~30% increase in immobility time (Fig. 6F). In the acoustic response assay, *Srrm2*$^{+/-}$

mice showed reduced startle responses across a broad range of startle frequencies (Fig. 6G); however, there was little impairment in prepulse inhibition (Fig. 6H).

Overall *Srrm2*$^{+/-}$ mice are characterized by generally reduced locomotor activity and abnormal responses in behavioral assays that are used to measure anxiety-like (center/margin distance) and depression-like behaviors (FST) in mice. Notably, these behavioral impairments (including increased immobility in FST, and deficits in acoustic startle, which is measured by force exerted (in Newtons) by the mouse in the analysis chamber) are also consistent with hypotonia (loss of muscle tone) a phenotype that is observed in humans with *SRRM2*- (5) and *SYNGAP1*-haploinsufficiency (24). In this context, it is notable that SynGAP-γ is the only SynGAP isoform that is robustly expressed in skeletal muscle (25).

EEG changes reminiscent of humans with SCZ in *Srrm2* mice

Sleep disturbances and EEG abnormalities are common in humans with SCZ (36, 37), and have been observed in genetic mouse models of SCZ (38). We therefore carried out 24-hour EEG recordings of *Srrm2*$^{+/-}$ mice and WT littermate controls at 3- and 6-months of age.

Automated sleep scoring (39) during 12-hour light-dark cycles showed no significant difference in time spent in NREM sleep, REM sleep, or wake between *Srrm2*$^{+/-}$ mutants and WT controls at 3 or 6 months of age (Fig. S6A).

Analysis of power spectral density during NREM sleep showed a widespread albeit non-significant attenuation in total EEG power (i.e. absolute power measured across all major frequency bands of brain oscillation) in S*rrm2*$^{+/-}$ mice (Fig. 7A, Fig. S6C). Power in the sigma band (10-15 Hz) was particularly robustly reduced in both parietal ($p=0.053$) and frontal ($p=0.026$) electrodes at 3-months of age (Fig. 7B, Fig. S6B).

The reduction in sigma band power in *Srrm2*$^{+/-}$ mice suggested reduced activity of sleep spindles, which are short bursts of 10-16 Hz oscillatory brain activity generated in the thalamus during NREM sleep (36). By analyzing sleep spindle events, we found that spindle occurrences (number of spindles per minute) (Fig. 7C, Fig. S6D), spindle duration (Fig. 7D, Fig. S6E), and spindle amplitude (Fig. 7E, Fig. S6F) were all substantially reduced in *Srrm2*$^{+/-}$ mice, with the reductions most robust in the parietal electrode at 3 months of age (Fig. 7C–E). Correspondingly, integrated spindle activity (ISA, a metric that combines both duration and amplitude) was strongly reduced at the parietal electrode of 3-month-old *Srrm2*$^{+/-}$ mice (Fig. 7F).

Sleep spindle occurrences, amplitude, and duration have consistently been found to be reduced (on average) in humans with SCZ (36, 37); *Srrm2*$^{+/-}$ mice therefore phenocopy core EEG abnormalities observed in SCZ. Intact spindles also correlate with cognitive function (36, 37); impaired spindle activity may therefore partly underlie the ID observed in humans with *SRRM2* LoF.

Discussion

We find that *Srrm2*$^{+/-}$ mice—an animal model of SCZ informed by human genetics—display several notable molecular and neurobiological phenotypes that overlap with abnormalities reported in humans with SCZ, such as negative impact on molecular pathways related to synapses, differential effects on activity-regulated genes in PFC (hypoactivity) and hippocampus (hyperactivity), dysregulated dopamine signaling in striatum and PFC, deficits of ODCs and myelination, and reduced occurrences of sleep spindles in EEG. Our findings

establish *Srrm2* heterozygous mutant mice as a new and useful model of SCZ and provide mechanistic insights into the pathophysiology of SCZ and the neurodevelopmental disorder associated with *SRRM2* LoF.

The splicing of messenger RNA is a fundamental step in gene expression, and is particularly affected in individuals with SCZ (12). It is therefore interesting that *SRRM2*, encoding an RNA splicing and processing factor, has emerged as a large-effect LoF risk gene for SCZ (2, 3). Notably, mutations in and cytoplasmic mislocalization of nuclear RNA binding proteins (ex. TDP43, FUS) are linked to frontotemporal dementia (40), a neurodegenerative disease that can present with psychosis (41, 42). Cytoplasmic mislocalization of SRRM2 itself—correlated with disruption in speckles and splicing—has recently been observed in the brains of humans with frontotemporal dementia and Alzheimer's disease (43, 44), suggesting that shared mechanisms involving disruptions to RNA regulation may underlie SCZ and multiple neurodegenerative diseases. In this context, it is notable that (i) several nuclear RNA binding proteins are elevated in synapse fractions of both *Srrm2*$^{+/-}$ (Fig. 2C, Fig. S2C) and *Grin2a*$^{+/-}$ models of SCZ (including Srrm2 itself in *Grin2a*$^{+/-}$ synapses) (45), and (ii) SCZ is considered to have a neurodegenerative component, especially later in life (46).

Consistent with Srrm2's central role in regulating gene expression, *Srrm2*$^{+/-}$ mice exhibit widespread changes in total gene expression (summed expression of all isoforms of a gene) across brain regions (Fig. 1). An interesting total gene expression change is that the activity-regulated gene set is reduced in PFC but elevated in HP and SSC. This pattern of changes in putative brain activity (as measured by activity-regulated genes) is consistent with neuroimaging findings from humans with SCZ (47, 48), and largely resembles the differential regional activity-regulated gene expression changes reported in *Grin2a*$^{+/-}$ mice (45). Large-scale changes are also observed in expression of mRNA isoforms of many genes (Fig. 3A), likely due to widespread alterations in splicing (Fig. 3E). Notably, analysis of total gene expression alone is insufficient—different isoforms of a gene can change in opposing directions and cancel each other out (Fig. 3C)—highlighting the need for a careful examination of isoform changes in each gene to fully understand the extent of gene expression changes.

Dysregulated dopamine signaling in the striatum is one of the prevailing hypotheses for SCZ (21). We find considerable evidence of abnormal dopamine signaling and/or circuitry in the striatum of *Srrm2*$^{+/-}$ mice, including: (i) elevated expression of dopamine signaling-related gene sets in bulk RNA-Seq, and (ii) increased proportion of D1 and D2 SPNs in the striatum determined from snRNA-seq analysis. The heightened expression of genes in the "response to dopamine" GO term in striatum bulk RNA (including *Htr2c*, *Drd1*, and *Drd2*; Fig. 1H) could reflect at least in part the increased proportions of D1/D2 SPNs in the striatum. In snRNA-seq measurements, D1 and D2 SPNs show downregulation of activity-regulated and dopamine-induced genes, implying reduced activity in these inhibitory neurons on average. Superficially, this does not align with a hyperdopaminergic state, which has been noted in SCZ patients (30, 49) and another SCHEMA mouse model (*Grin2a*$^{+/-}$) (45). Further neurophysiological investigation of the striatum will help to decipher the dopaminergic circuit dysfunction in *Srrm2* mutant mice.

Studies of both common and rare genetic variants (2, 20), as well as of postmortem brain tissue (16, 50), have consistently pointed to dysregulation of synapses as a central pathomechanism in SCZ. We find (by transcriptomics and proteomics) that *Srrm2*, even though it encodes a protein localized in nuclear speckles, has profound effects on synapses. In *Srrm2*$^{+/-}$ mice, by bulk RNA-seq, synapse-related gene sets are downregulated in all brain regions examined except for SSC, where they are upregulated, implying a differential region-specific

impact on synapses, as previously shown for the *Grin2a*$^{+/-}$ model of SCZ (45). By proteomics, we find that many key postsynaptic density (PSD) proteins are reduced in synapse fractions of adult *Srrm2*$^{+/-}$ mice—most prominently, the gamma isoform of SynGAP. In addition to regulating synaptic signaling, SynGAP is thought to play a structural role at the PSD, where it is highly concentrated (estimated concentration of ~100 μM) (51, 52). It is therefore possible that the reductions of other key PSD proteins—several of which (Anks1b, Iqsec1, Iqsec2) are known to bind SynGAP (23, 53)—is driven in part by the loss of structural support conferred by SynGAP-γ (54).

Notably, heterozygous LoF mutations in *Syngap1* cause a syndrome characterized by ID, developmental delay, and autism—phenotypes that are also observed in humans with *SRRM2* haploinsufficiency (5, 24). A judicious interpretation of this similarity is therefore that shared mechanisms underlie the *SYNGAP1*- and *SRRM2*-LoF disorders, and that the reduction in SynGAP-γ contributes to the phenotypes observed with *SRRM2* LoF. We note that SynGAP-γ isoform likely constitutes a minor portion of total SynGAP protein in the brain (25), which may explain why such a large reduction (~70%) is tolerated without lethality in *Srrm2*$^{+/-}$ mice.

What causes the depletion of SynGAP-γ? We find that the full-length isoform of Agap3 (Agap3-FL) is markedly elevated in *Srrm2*$^{+/-}$ brains, and this can be parsimoniously explained by abnormal splicing of *Agap3* mRNA due to deficiency of Srrm2 (an RNA splicing protein). Because Agap3 is a known binding partner of SynGAP, and since there was no obvious disturbance of SynGAP splicing, the marked anti-correlation between Agap3 and SynGAP-γ levels strongly suggests that the increase in Agap3-FL levels causes the reduction in SynGAP-γ levels at the synapse. Further investigations into the nature of Agap3-SynGAP interaction should shed light on these molecular mechanisms.

Altered myelination is an emerging theme in the pathology of SCZ (55) and other CNS disorders (56, 57). Neuroimaging (58), histopathological (29), transcriptomic (12), and genomic (59) studies have noted deficits in (i) ODC numbers, (ii) ODC- and myelin-related gene and/or protein expression, and (iii) myelination in the brains of humans with SCZ. In unbiased studies of *Srrm2*$^{+/-}$ mice, we report reductions in ODC numbers and in myelin-related gene and protein expression in multiple regions of the brain. Thus, *Srrm2* heterozygous LoF mice phenocopy several cellular and molecular features of ODC depletion and reduced myelination seen in SCZ patients, raising the possibility that therapeutic strategies to increase myelination and/or ODC numbers may be beneficial in some subsets of SCZ. In this context, we note that in PheWAS of UK biobank exomes, *SRRM2* LoF is most strongly associated with myelination compared to all other phenotypes—albeit with moderate *P*-values (~10^{-4}) (60). Overall, our study illustrates the power of comprehensive and unbiased multi-omics analyses for gaining insights into the molecular and neurobiological mechanisms of complex psychiatric diseases.

Figure Legends

Fig. 1: **Large-scale and correlated transcriptomic changes across different brain regions in *Srrm2*$^{+/-}$ mice.** (A) Number of DEGs (*Srrm2*$^{+/-}$ vs. WT) in the profiled brain regions at 1- and 3-months of age. Correlation of gene expression changes (log2FC) in 1-month-old *Srrm2*$^{+/-}$ mice transcriptome-wide (B), and (C) in the 6429 genes that are DE (FDR-adjusted $P < 0.05$) in any of the brain regions. (D) Evaluation of gene expression changes (log2FC) in the PFC against those in the striatum (ST) in 1-month-old *Srrm2*$^{+/-}$ mice. (E) Heatmap showing log2FCs of genes of interest that are DE in at least 4 brain regions in 1-month-old *Srrm2*$^{+/-}$ mice. Also shown are *Chrm1/4* and *Nptx2*. Stroked cells indicate DE in the indicated brain region. GSEA results

showing enrichment of various molecular pathways from (F) mSigDb, and (G) SynGO and psychiatric disease-associated gene sets. (H) Evaluation of gene expression changes (log2FC) against *P*-value in the striatum of 1-month-old *Srrm2*$^{+/-}$ mice; genes in the "response to dopamine" pathway are highlighted. Horizontal dotted line indicates FDR-adjusted *P*-value threshold of 0.05.

Fig. 2: ***Srrm2* LoF causes isoform-specific changes in SynGAP and Agap3 at the synapse**. Volcano plots showing (A) DEPs in 1- and (B) 4-month-old *Srrm2*$^{+/-}$ mice synapses. (C) GSEA results highlighting prominently changed pathways in SynGO and mSigDB in the cortical synapse proteome of *Srrm2*$^{+/-}$ mice. (D) Volcano plot of synapse proteome changes in 4-month-old *Srrm2*$^{+/-}$ mice, highlighting all proteins in the SynGO "postsynaptic density intracellular component" gene set. (E) Evaluation of log2FCs in 1-month-old *Srrm2*$^{+/-}$ mice synapses against those in 4-month-old *Srrm2*$^{+/-}$ mice. Protein isoforms of SynGAP and Agap3 are highlighted. (F) Western blots showing levels of SynGAP-γ, Agap3-FL, Crag, and SynGAP-A1 in synapse fractions from 1-month-old *Srrm2*$^{+/-}$ mice and WT littermates. (G) Quantifications of (F). Error bars indicate standard error of the mean (SEM).

Fig. 3: **Altered *Agap3* mRNA splicing across the brain of *Srrm2*$^{+/-}$ mice.** (A) Each boxplot shows distributions of gene-level *P*-values of transcriptomic differences (*Srrm2*$^{+/-}$ vs. WT) in the labeled brain region and age. *P*-values from isoform-level analysis of each gene were aggregated to obtain the gene-level results. Counts of individual mRNA isoforms of *Agap3* in (B) the PFC of 1-month-old *Srrm2*$^{+/-}$ mice, and (C) across all 8 brain regions in both 1- and 3-month-old mutant mice and WT littermates. (D) Gene models showing exonic and intronic regions of the six Ensembl-annotated *Agap3* isoforms. (E) Boxplot showing distributions of intron-cluster *P*-values of Leafcutter splicing analysis for 1- (top) and 3-month-old (bottom) *Srrm2*$^{+/-}$ mice. *P*-values of Indicated clusters are highlighted. (F) Gene model highlighting splicing changes in *Agap3* found by Leafcutter. (G) Quantification of Agap3 and SynGAP-γ protein levels in the P2 fractions and total extracts of indicated brain regions of *Srrm2*$^{+/-}$ mice and WT littermates. (H) Representative western blot of Agap3 in P2 fractions of the *Srrm2*$^{+/-}$ mice hippocampus. (I) Evaluation of MS/MS abundances of Agap3-FL compared to those of SynGAP-γ. Error bars indicate SEM throughout.

Fig. 4: **Reduced oligodendrocyte numbers, and decreased expression of myelin-related mRNAs and proteins in *Srrm2*$^{+/-}$ mice.** (A) UMAP representation of the major cell types identified by snRNA-seq in the indicated brain regions of WT and *Srrm2*$^{+/-}$ mice. Cell type proportions of nuclei profiled from (B) PFC and (C) striatum of 1-month-old *Srrm2*$^{+/-}$ mice and WT littermate controls (Inhib.N = inhibitory neurons, Excit.N = excitatory neurons, Astro. = astrocytes, ODC = oligodendrocytes). Error bars indicate SEM. (D) Evaluation of proportion of inhibitory neurons against those of ODCs (in percentages) in 1-mo striatum of *Srrm2*$^{+/-}$ mice and WT littermates. (E) Bubble plot showing bulk RNA-Seq GSEA results for the "myelin sheath" gene set in 8 brain regions of 1- and 3-mo *Srrm2*$^{+/-}$ animals. (F) Evaluation of cortical synapse proteome changes in 1-month-old *Srrm2*$^{+/-}$ mice. Downregulated proteins with $P < 0.05$ that were also found to show ODC enrichment in Allen Brain Atlas are highlighted. Also highlighted is Mobp. (G) Volcano plot of cortical synapse proteome changes in 4-month-old *Srrm2*$^{+/-}$ mice. The same set of proteins highlighted in (F) are highlighted. (H) Quantification of western blots examining changes in CNPase and Mbp in total extracts ("Ctx" = cortex) or synapse fractions ("Syn.") in the indicated brain regions. Error bars indicate SEM. (I) Boxplot showing distributions of gene-level *P*-values of transcriptomic differences (*Srrm2*$^{+/-}$ vs. WT) in 1- and 3-month-old *Srrm2*$^{+/-}$ brains; aggregate *P*-values of *Qki* are highlighted.

Fig. 5: ***Srrm2* LoF causes pervasive gene expression changes in neuronal and glial cells.** (A) Number of DEGs across cell types in 1-month-old PFC and striatum of *Srrm2*$^{+/-}$ mice. (B) Molecular pathway changes as measured by GSEA across cell types in PFC and striatum of 1-month-old *Srrm2*$^{+/-}$ mice. (C) Evaluation of log2FC vs. *P*-value in inhibitory neurons of the striatum of 1-month-old *Srrm2*$^{+/-}$ mice; the genes that constitute activity-regulated genes and dopamine-induced genes, as well as those that belong to both, are highlighted.

Fig. 6: **Behavioral abnormalities in *Srrm2*$^{+/-}$ mice.** (A) Total running wheel distance of *Srrm2*$^{+/-}$ mice and WT littermate controls (n=9 WT, 8 *Srrm2*$^{+/-}$). (B)—(E) Performance of *Srrm2*$^{+/-}$ in open field testing (n=17 WT, 16 *Srrm2*$^{+/-}$); (B) Distance traveled against time; distance is averaged in 5 min bins. (C) Total distance traveled summed over the duration of the assay. (D) Total jump counts. (E) Ratio of total distance traveled in the center to that in the margin. (F) Immobility time (in seconds) in the forced swim test (n= 15 WT, 15 *Srrm2*$^{+/-}$). (G) Auditory startle (Force, in newtons) and (H) percent inhibition of auditory startle reflex with the application of pre-pulse of indicated dB in the auditory startle test (n= 14 WT, 14 *Srrm2*$^{+/-}$). Error bars indicate SEM throughout. Student's T-test or one-way ANOVA F-test *P*-values testing for genotype differences are shown.

Fig. 7: **EEG changes reminiscent of humans with SCZ in *Srrm2*$^{+/-}$ mice.** 17 WT and 13 *Srrm2*$^{+/-}$ animals were used for all EEG analyses. (A) Absolute power of indicated frequency bands during NREM sleep in electrodes implanted in the parietal cortex of 3-month-old *Srrm2*$^{+/-}$ mice, compared to those in WT littermate controls. Linear-mixed effects model *P*-values testing for genotype difference in total power across all bands is shown. (B) Total sigma power in parietal and frontal cortex during NREM sleep at 3-months of age in *Srrm2*$^{+/-}$ mice and WT littermate controls; linear-mixed effects model *P*-values testing for difference in genotype are shown. Sleep spindle occurrences (number of spindles per minute) (C), spindle duration (D), spindle amplitude (E), and (F) integrated spindle activity in parietal cortex of 3-month-old *Srrm2*$^{+/-}$ mice, compared to WT littermates. Spindles are segregated by frequency bands. Linear mixed-effects model *P*-values testing for genotype difference, as well as pairwise differences in each frequency band are shown. Error bars indicate SEM throughout.

Fig. S1: **Large-scale and correlated transcriptomic changes across different brain regions in *Srrm2*$^{+/-}$ mice.** (A) Sanger sequencing of the deletion in exon 9 of the *Srrm2* locus. del = deletion. endo = endogenous. Bottom panel shows a magnification of exon 9. The del primers skip the deleted region, while the endo primers sequence through; the endo primers nevertheless sequence poorly because of the homopolymeric sequence of the deleted region. (B) PCR amplification of the deletion. The deletion results in a smaller amplification product. (C) The 8 brain regions that were dissected (left) and evaluation of the first two principal components of RNA-Seq datasets from those brain regions of 1- and 3-month-old *Srrm2*$^{+/-}$ mice and WT littermate controls (right). (D) Normalized counts of the *Srrm2* gene in all profiled brain regions in 1- and 3-month-old WT and *Srrm2*$^{+/-}$ mice. (E) Representative RNA-Seq read density in the *Srrm2* locus in the PFC of 1-month-old *Srrm2*$^{+/-}$ mice and WT littermate controls. The *Srrm2* exon 9 deletion causes substantial reduction in reads aligning to the *Srrm2* across its gene body. Number of shared DEGs across number of brain regions in (F) 1- and (I) 3-month-old *Srrm2*$^{+/-}$ mice. Indicated number is not cumulative (i.e. 40 genes DE in exactly 7 brain regions does not include the 28 genes DE in all 8 regions). (G) Heatmap showing gene expression changes (log2FCs) in genes that are DE across all 8 brain regions in 1-month-old *Srrm2*$^{+/-}$ mice. (H) Heatmap of log2FCs in the 1299 genes DE across exactly two brain regions in 1-month-old *Srrm2*$^{+/-}$ mice. Correlation of gene expression changes in 3-month-old *Srrm2*$^{+/-}$ mice (I) transcriptome-wide, and (K) in the 1640 genes that are DE in any of the brain regions.

(L) Heatmap showing log2FCs in genes that are DE in 4 or more brain regions in 3-month-old *Srrm2*$^{+/-}$ mice. Only genes detected across all 8 brain regions are included in heatmap (for purposes of hierarchical clustering).

Fig. S2: ***Srrm2* LoF causes isoform-specific changes in SynGAP and Agap3 at the synapse**. (A) Volcano plot showing cortical synapse proteome changes in 4-month-old *Srrm2*$^{+/-}$ mice. Members of the SynGO "postsynaptic density membrane" set are highlighted. (B) Evaluation of log2FCs in 1-month-old *Srrm2*$^{+/-}$ synapses vs. those in 4-month-old synapses. The individual components of the "postsynaptic density" set are highlighted. The majority of these proteins are reduced at 4-months of age, but not at 1-month. (C) Heatmap showing log2FCs in ribosomal proteins and RNA-binding proteins in 1- and 4-month-old *Srrm2*$^{+/-}$ mice synapses. Stroked cells indicate DEPs. Proteins with *P*-values < 0.1 in 1- or 4-month-old synapses (*Srrm2*$^{+/-}$ vs. WT) are labeled. (D) Multiple sequence alignment of the four C-terminal isoforms of the SynGAP protein. (E) Multiple sequence alignment of the protein isoforms of Agap3.

Fig. S3: **Altered *Agap3* mRNA splicing across the brain of *Srrm2*$^{+/-}$ mice.** (A) Gene expression changes (log2FC) in *Syngap1* and *Agap3* across brain regions. Stroke indicates DE. (B) Nominal *P*-value distributions of the 6 transcript isoforms of *Agap3* across brain regions in 1- and 3-month-old *Srrm2*$^{+/-}$ mice. (C) Western blot examining Agap3-FL and SynGAP-γ levels in P2 fractions of the cerebellum, hippocampus, and striatum of *Srrm2*$^{+/-}$ mice and WT littermate controls. The cortical synapse fraction (labeled "cortex PSD") serves as a positive control.

Fig. S4: **Reduced oligodendrocyte numbers, and decreased expression of myelin-related mRNAs and proteins in *Srrm2*$^{+/-}$ mice.** (A) Cell type proportion changes in inhibitory neuron types of the striatum of 1-month-old *Srrm2*$^{+/-}$ mice. FDR-adjusted *P*-values testing for differences in proportions of cell types between WT and *Srrm2*$^{+/-}$ mice are indicated. (B) The numbers of each major cell type (including total number profiled) identified by snRNA-seq in the striatum of 1-month-old *Srrm2*$^{+/-}$ mice. One-way ANOVA F-test *P*-value testing for difference in ODC numbers is indicated. (C) Bubble plot showing bulk RNA-Seq GSEA results for the "Lein_oligodendrocyte_marker" mSigDB gene set in 8 brain regions of 1- and 3-mo *Srrm2*$^{+/-}$ animals. (D) Evaluation of cell type specific gene expression of the 27 reduced DEPs in 1-month-old *Srrm2*$^{+/-}$ synapses in the Allen Cell Types database. Of the 27, the expression of 26 was available in the database. 10 of the 26 are enriched in ODCs (highlighted in red). (E) Western blot of Mbp and CNPase in striatal total extracts of WT and *Srrm2*$^{+/-}$ mice (n=6 each). A representative section of total protein (the loading control) and an unchanged protein (β-Actin) is also shown. (F) Gene models showing exonic and intronic regions of the six *Qki* isoforms. (G) Counts of the six Ensembl-annotated isoforms of *Qki* in the striatum of 1-month-old *Srrm2*$^{+/-}$ mice.

Fig. S5: **Behavioral abnormalities in *Srrm2*$^{+/-}$ mice.** Evaluation of novel object recognition by *Srrm2*$^{+/-}$ mice and WT littermate controls after (A) 10 minutes, and (B) 24-hours of introduction to the object. (C) Evaluation of 3-chamber social interaction and (D) social recognition in *Srrm2*$^{+/-}$ mice, compared to WT littermate controls. (E) Evaluation of performance of *Srrm2*$^{+/-}$ mice in the Y-maze assay of spatial memory. Evaluation of (F) average home cage activity (over 1 month) and (G) average home cage activity over the duration of a day, across 30 days, in WT (left) and *Srrm2*$^{+/-}$ mice (right). Error bars indicate SEM throughout. Student's T-test *P*-values testing for genotype differences are shown.

Fig. S6: **EEG changes reminiscent of humans with SCZ in *Srrm2*$^{+/-}$ mice.** 17 WT and 13 *Srrm2*$^{+/-}$ animals were used for all EEG analyses. (A) Time spent in REM or NREM sleep and wake (in hours) by *Srrm2*$^{+/-}$ mice and WT littermate controls. Two-way ANOVA F-test *P*-value

testing for genotype difference is shown. (B) Total sigma power in parietal and frontal cortex during NREM sleep at 6-months of age in *Srrm2*$^{+/-}$ mice and WT littermate controls; linear-mixed effects model *P*-values testing for difference in genotype are shown. (C) Absolute power of indicated frequency bands during NREM sleep in electrodes implanted in the indicated brain region at the indicated age in *Srrm2*$^{+/-}$ mice, compared to those in WT littermate controls. Linear-mixed effects model *P*-values testing for genotype difference in total power across all bands is shown. Sleep spindle occurrences (number of spindles per minute) (D), spindle duration (E), and spindle amplitude (F) in the indicated brain region in 3- and 6-month-old *Srrm2*$^{+/-}$ mice, compared to WT littermates. Spindles are segregated by frequency bands. Linear mixed-effects model *P*-values testing for genotype difference, as well as those testing for pairwise differences are shown.

Methods

Experimental model and subject details

Srrm2 mutant mice

We used the *Srrm2* $^{em1(IMPC)Bay}$ mouse line in this study. This line was generated by the knockout mouse program (KOMP) / International Mouse Phenotyping Consortium (IMPC) at Baylor College of Medicine (Houston, TX) (14). *Srrm2* $^{em1(IMPC)Bay}$ mice harbor a deletion (introduced by the Cas9-RNA guided nuclease) of exon 9 in the mouse *Srrm2* gene.

Cryopreserved germplasm (sperm samples) heterozygous for the *Srrm2* $^{em1(IMPC)Bay}$ allele were obtained from John Seavitt (Baylor College of Medicine) and mutant mice were re-derived by in-vitro fertilization at Harvard Genome Modification Facility (Cambridge, MA). Mutant mice were back-crossed with C57BL/6J (The Jackson Laboratory, #000664) for two generations, after which female mutant mice were bred with C57BL/6J males to generate experimental animals (*Srrm2*$^{+/-}$ and WT littermates). To minimize genetic drift, breeders were periodically refreshed by pairing fresh ~4-month-old *Srrm2* $^{em1(IMPC)Bay}$ mutant females with freshly obtained C57BL/6J males from the Jackson Laboratory.

Mice were housed in AAALAC-approved facilities on a 12-hour light/dark cycle, with food and water available *ad libitum*. All procedures involving mice were approved by the Broad Institute IACUC (Institutional Animal Care and Use Committee) and conducted in accordance with the NIH Guide for the Care and Use of Laboratory Animals.

Male mice were used for biochemical and molecular studies (RNA-Seq, proteomics, synapse fractionation, western blotting), as well as for EEG studies. Both male and female mice were used for behavioral studies.

Method details

Brain perfusion and dissection

Mice were transcardially perfused under 3% isoflurane anesthesia with Hank's Balanced Salt Solution (HBSS). The perfused brains were dissected, frozen in liquid nitrogen vapor, and stored at -80°C as described in detail in (61). Brain regions were dissected on a cryotome (Leica CM3050S) as described in (45).

RNA isolation and bulk RNA-seq library preparation

Dissected brain tissue was lysed, and total RNA isolated using RNeasy Mini Kit (Qiagen) following the manufacturer's instructions. RNA concentration was measured using Nanodrop, and RNA quality / RNA integrity number assessed using High Sensitivity RNA Electrophoresis chips on an Agilent Bioanalyzer. Isolated total RNA was stored at -80°C until bulk RNA-Seq library preparation.

Bulk RNA-Seq cDNA libraries were prepared using a TruSeq Stranded mRNA Kit (Illumina). The fragment sizes of the cDNA libraries were analyzed using High Sensitivity DNA chips (Agilent) on a 2100 Bioanalyzer Instrument (Agilent), and their concentrations measured using Qubit fluorometer. A 10 nano molar (nM) normalized library was pooled, and paired-end sequencing was performed on a NovaSeq S2 (Illumina) with 50 bases each for reads 1 and 2 and 8 bases each for index reads 1 and 2.

Bulk RNA-Seq libraries were prepared from 5 WT and 5 *Srrm2*$^{+/-}$ mice for each brain region and age. Three 3-month SN samples (1 WT and 2 *Srrm2*$^{+/-}$) were excluded from sequencing due to failure in library preparation.

Total extract preparation and purification of synaptic and P2 fractions

Mice were euthanized using CO_2 inhalation after which the cortex, hippocampus, and cerebellum were rapidly dissected, flash-frozen in liquid nitrogen, and stored at -80°C until further processing.

Frozen brain tissue was thawed and dounce-homogenized in ice-cold homogenization buffer (5 mM HEPES pH 7.4, 1 mM $MgCl_2$, 0.5 mM $CaCl_2$, supplemented with phosphatase and protease inhibitors).

For total extract preparation, sodium dodecyl sulfate (SDS) was added to the homogenate to a final concentration of 2%. The extract was sonicated (using a probe sonicator), clarified (at 15,000 g for 10 minutes at room temperature), and the supernatant collected.

For P2 fraction preparation, instead of adding SDS, the homogenate was centrifuged for 10 minutes at 1,400 g (4°C) and the supernatant was re-centrifuged at 13,800 g for 10 minutes (4°C). The resulting pellet–-which is enriched in synaptosomes and mitochondria—was resuspended in 0.32 M Sucrose, 6mM Tris-HCl (pH 7.5) to obtain the P2 fraction.

For synaptic fractions, the P2 fraction was layered gently on a 0.85 M, 1 M, 1.2 M discontinuous sucrose gradient (in 6 mM Tris-HCl pH 8.0) and ultracentrifuged at 82,500 g for 2 hours (4°C). The synaptosome fraction—which sediments at the 1 M and 1.2 M sucrose interface—was collected and an equal volume of ice-cold 1% Triton X-100 (in 6 mM Tris-HCl pH 8.0) was added. After incubating on ice for 15 minutes, this mixture was ultracentrifuged at 32,800 g for 20 minutes (4°C), and the final synapse fraction pellet (also called postsynaptic density fraction) was collected by resuspension in 1% SDS. A small aliquot was taken to measure the protein concentration using the micro BCA assay (Thermo Fisher), and the remaining protein was stored at -80°C until being processed for mass spectrometry or western blotting.

Processing of synaptic fractions for mass spectrometry

Eighteen synaptic fractions from WT and *Srrm2*$^{+/-}$ mouse cortices were analyzed using tandem mass tag (TMT) isobaric labeling for quantification (1-mo WT n = 4, 1-mo *Srrm2*$^{+/-}$ n = 5, 4-mo WT n = 5, 4-mo *Srrm2*$^{+/-}$ n = 4).

The protein in synapse fraction samples (in 1% SDS) was reduced using 5 mM dithiothreitol and alkylated using 10 mM iodoacetamide at room temperature. The denatured, reduced, alkylated protein samples were then processed using S-Trap sample processing technology (Protifi) following manufacturer's instructions. The proteins were bound to the S-Trap column via centrifugation and contaminants/detergents were washed away. Sequential digestion steps were then performed on column using 1:20 enzyme to substrate ratio of Lys-C for 2 hours and Trypsin overnight at room temperature.

Following digestion and desalting, 15 µg of each sample was labeled with TMT18 reagent; the TMT18 plex was constructed by randomly assigning the samples from each group to channels within the plex. After verifying successful labeling of more than 99% label incorporation, reactions were quenched using 5% hydroxylamine and pooled. The TMT18 labeled peptides were desalted on a 50 mg tC18 SepPak cartridge and fractionated by high pH reversed-phase chromatography on a 2.1 mm x 250 mm Zorbax 300 extend-c18 column (Agilent). One-minute fractions were collected during the entire elution and fractions were concatenated into 12 fractions for LC-MS/MS analysis.

One microgram of each proteome fraction was analyzed on a Exploris 480 QE mass spectrometer (Thermo Fisher Scientific) coupled to a Vanquish Neo LC system (Thermo Fisher Scientific). Samples were separated using 0.1% Formic acid / Acetonitrile as buffer A and 0.1% Formic acid / Acetonitrile as buffer B on a 27cm 75um ID picofrit column packed in-house with Reprosil C18-AQ 1.9 mm beads (Dr Maisch GmbH) with a 90 min gradient consisting of 1.8-5.4% B in 1 min, 5.4-27% B for 84 min, 27-54% B in 9 min, 54-81% B for 1 min followed by a hold at 81% B for 5 min. The MS method consisted of a full MS scan at 60,000 resolution and a normalized AGC target of 300% and maximum inject time of 10ms from 350-1800 m/z followed by MS2 scans collected at 45,000 resolution with a normalized AGC target of 30% with a maximum injection time of 105 ms and a dynamic exclusion of 15 seconds. Precursor fit filter was used with a threshold set to 50% and window of 1.2 m/z. The isolation window used for MS2 acquisition was 0.7 m/z and 20 most abundant precursor ions were fragmented with a normalized collision energy (NCE) of 34 optimized for TMT18 data collection.

Western blotting

Total extracts, P2 fractions, and synaptic fractions were prepared as described, and their protein concentrations measured using Bicinchoninic acid assay (BCA; Thermo Fisher). Laemmli buffer (6X; Boston Bioproducts BP-111R) was added to the samples at a final concentration of 1X, and the samples heated at 95°C for 5 minutes.

SDS-PAGE was carried out by electrophoresing the samples on a denaturing 4-12% NuPage gradient gels (Thermo Fisher). Gels were transferred to nitrocellulose membranes (Bio-Rad TransBlot Turbo), and total protein staining (LiCor 926-11010) was performed. Membranes were then blocked with 5% milk in Tris-buffered saline with 0.1 % Tween 20 (TBST). Membranes were incubated with primary antibodies overnight at 4C, washed three times with TBST, and then incubated with secondary HRP-conjugated antibodies for 1-2 hours at room temperature. After additional washing (4 X 5 minutes), membranes were imaged on ChemiDoc XRS+ (Bio-Rad) and analyzed using Image Lab Software (Bio-Rad).

The antibodies used were as follows: Mbp (Biolegend 808401), CNPase (Biolegend 836404), Pak4 (Cell Signaling 62690), Gpt (ProteinTech 16897-1-AP). Isoform-specific SynGAP (25) and Agap3 (27) antibodies were a kind gift from Yoichi Araki (Johns Hopkins).

Nuclei purification and snRNA-seq library preparation

Nuclei were purified by dissociating dissected brain tissue in a 1% Triton-X based buffer, followed by FACS enrichment, as detailed in (62). Purified nuclei were loaded on a 10x Chromium v3.1 system (10x Genomics) and library preparation (Single Cell 3'; 10X Genomics) was performed according to the manufacturer's protocol. cDNA fragment sizes were analyzed using High Sensitivity DNA chips (Agilent), a 10 nM normalized library was pooled, and sequencing performed on a NovaSeq S2 (Illumina) with 28 and 75 bases for reads 1 and 2 and 10 bases each for index reads 1 and 2.

snRNA-Seq libraries were prepared from 6 WT and 6 *Srrm2*$^{+/-}$ mice for each brain region.

EEG implantation and recording

EEG electrodes were implanted as described previously (38, 45). Briefly, 8- to 10-week-old mice (n = 13 WT and 17 *Srrm2*$^{+/-}$) were deeply anesthetized with isoflurane. A prefabricated EEG/EMG headmount (#8201SS, Pinnacle Technology, Lawrence, KS) was secured to the skull with four 0.10" intracranial electrode screws (#8403, Pinnacle Technology) at the following stereotactic coordinates: parietal recording electrode (-1.5 AP, 2.0 ML to Bregma), frontal recording electrode (1.5 AP, 1.5 ML to Bregma), and ground and reference electrodes (bilaterally -1 AP, 2 ML to Lambda). The electromyogram (EMG) electrodes were placed bilaterally in the nuchal muscles. Electrodes were soldered to the EEG/EMG head-mount and dental acrylic was used to secure the connections. Animals were given at least two weeks of post-operative recovery before EEG recording. Following recovery from EEG implantation, mice were tethered to the Pinnacle recording system, with at least 24 hours of habituation before recording. For sleep/wake recordings, EEG/EMG signals were recorded for 24 hours from the onset of the dark phase, ZT12 (6 pm EDT or 7 pm EST). Animals remained tethered to the Pinnacle system throughout the testing period with *ad libitum* access to food and water. All signals were digitized at a sampling rate of 1000 Hz, filtered (1–100 Hz bandpass for EEG; 10–1 kHz bandpass for EMG), and acquired using the Sirenia Acquisition program (Pinnacle Technology). EEG recordings were carried out at ~3- and ~6-months of age.

Behavior profiling

Investigators were blinded to the genotypes for all behavioral tests.

Homecage locomotor activity monitoring

Mice were transferred to Digital Ventilated Cages (DVC, Tecniplast) and were single housed throughout the duration of the experiment. Briefly, DVC racks use 12 electrodes beneath each cage that radiates an electromagnetic field that can detect disturbances that correlate with animal movement. The DVC Analytics web platform was used to generate animal locomotor indices, which calculate the percentage of 12 electrodes that measured movement over a 1-minute bin. For the locomotor activity index, a value of 1 means 12 electrodes measured movement, and a value greater than 1 means that there were more than 12 detected movements. A running wheel was added to the cage in the final week of the experiment.

Open field

Mice were monitored using the SuperFlex Open Field system (40 cm x 40 cm x 40 cm; Omnitech Electronics, Inc., Columbus, OH) for 60 minutes. The animals' position was captured

in real time using Fusion system software (Omnitech Electronics, Inc.). Total distance traveled, center/margin distance, and jump counts were calculated using the system's inbuilt software. The center was defined as the central 8 x 8 squares (of a 16 X 16 matrix) plus the coordinates between the outermost beams of the area and the adjacent non-area beams, whereas the margin was defined as the exterior 4 x 16 and 16 x 4 matrices for the left, right bottom and top regions of the arena.

Forced swim test

Mice were placed gently by their tail in a 4-liter Griffin beaker filled two-thirds with water maintained at room-temperature (24°C ± 1°C) for 6 minutes, and the amount of time the mice spent immobile was recorded. The temperature was tested before each test with an infra-red or glass thermometer.

Acoustic startle and PPI

To test acoustic startle, the test mouse was placed in a sound-attenuating chamber on a motion-sensitive platform. The background noise was set at 60 dB. After a 5-minute period of acclimation, a series of sudden, loud acoustic stimuli of 60, 70, 80, 85, 90, 95, 100, 105, 115 dB were presented in random order. For PPI, mice were exposed to 20 millisecond-long pre-pulses of 74, 78, 82, 86, 90 or dB. 100 milliseconds after the pre-pulse, mice were exposed to a constant startle tone of 105 dB that lasted 40 milliseconds. For both tests, the intertrial interval, which was randomly chosen, was 10, 15, 20, 25, or 30 seconds. For each stimulus, 5 trials were performed (in random order, with random order of inter-trial interval). The startle response was recorded as the force exerted by the mouse in response to each acoustic stimulus. The recording time was set to 250 milliseconds. The percentage of prepulse inhibition of the startle response was calculated as 100 × [startle response$_{(pre\text{-}pulse)}$ – (startle response$_{(prepulse + pulse)}$]/startle response$_{(pre\text{-}pulse)}$.

Novel objection recognition

Novel object recognition testing was performed in a 30 cm (w) X 30 (l) X 10 (h) arena made of acrylic. To reduce anxiety in the animals, light in the testing area was dimmed to 30 ± 5 lux. The testing was conducted over two days. On day 1 mice were habituated to the empty arena for 15 minutes. On day 2 mice were exposed to two identical objects in the rear left and right corners of the arena for 10 minutes. The mice were then returned to their home cages. After 10 minutes or 24 hours, mice were returned to the test arena with one of the familiar objects in place and a novel object of the same size in the same area as the other familiar object. The amount of time the mice spent interacting with the novel and familiar objects was recorded; testing was carried out for a period of 5 minutes. The arena and objects were cleaned between trials to prevent odor cues. Animal tracking and object exploration scoring was performed with Ethovision XT17 (Noldus).

Social interaction and social novelty

Social interaction and preference for novel animals were evaluated using the standard 3-chambered apparatus, which consists of a central chamber connected to two side chambers. Mice were placed in the central chamber and allowed to explore all three chambers freely for five minutes to habituate to the arena. After the habituation period, an unfamiliar male mouse that had no prior contact with the test mouse, was placed in one of the side chambers enclosed in a small round wire cage. An identical empty wire cage (the "object") was placed in the other

chamber. The animals serving as strangers were male mice that had previously been habituated to placement in the small cage. Both doors to the side chambers were then unblocked and the test mouse was allowed to explore the entire arena for a 10-minute session. The amount of time spent investigating the stranger mouse by the test mouse was recorded manually using a stopwatch. Social interaction was quantified by (time spent interacting with the mouse) / (time spent interacting with mouse + time spent interacting with object). After a 10-minute trial, a second stranger mouse was placed in the empty wire cage. The amount of time spent investigating each of the mice by the test mouse was recorded manually, and preference for novel animals was calculated as (novel mouse time) / (novel mouse time + familiar mouse time).

Y-maze

Forced alternation tests were conducted using a symmetrical Y-maze, which consists of a starting arm, an open arm, and a novel/blocked arm. Each arm of the Y-maze was 35 cm long, 5 cm wide and 10 cm high. Mice were habituated to the testing room for at least 30 min. Following habituation, mice were placed in the starting arm and allowed to explore two arms (starting and open) of the Y-maze for 10 minutes, while the entrance to the third arm was blocked. After the sample trial, the mouse was returned to its home cage for a 30 min inter-trial interval. The block in arm 3 was then removed and the mouse was placed into the starting arm again and allowed access to all three arms of the maze for five minutes. Mice were required to enter an arm with all four paws in order for it to be counted as an entry. The time spent in the novel arm was calculated as a percentage of the total time in novel and open arms during the 5-min retrieval trial. The maze was cleaned between trials.

Quantification and statistical analysis

Bulk RNA-seq gene DE

RSEM v1.3.084 (63) was used to estimate gene and isoform expression values. The M25 (GRCm38.p6) GENCODE reference was generated using RSEM-prepare-reference with default parameters. Expression values were calculated using RSEM-calculate-expression with the following flags: –bowtie2, –paired-end, –estimate-rspd, –append-names, and –sort-bamby-coordinate. *DESeq2* v1.20.0 (64) was used to perform DE analysis for each brain region and age. For comparisons of normalized counts across regions and age, all samples of every region and age were read into a single DESeq object. Log2FC values were adjusted using DESeq2's *lfcShrink* function with the 'normal' shrinkage estimator.

Bulk RNA-seq isoform DE and P-value aggregation

Reads were pseudoaligned to the Gencode M32 transcriptome using *Kallisto* 0.46.1 (65), with the number of bootstraps set to 50. Isoform-level DE analysis was performed using *Sleuth* 0.30.1 (66) by comparing a full model (with genotype as the only parameter) with a reduced model for each brain region and age. *P*-values generated by the isoform DE tests for each gene were aggregated (meta-analyzed) using the Lancaster method, as described in Yi et al. (28), also using *Sleuth*. Gene-level mRNA abundance estimates do not fully capture the dynamics of its constituent isoforms. For example, the abundance of different isoforms of the same gene changing in opposite directions can cancel each other out and lead to minimal changes in overall mRNA abundance (the sum of the abundances of constituent isoforms). In such a case, the aggregation of the *P*-values of each constituent isoform—which is performed

by this method—results in an even lower *P*-value thereby unmasking and prioritizing genes with dynamic effects among its multiple constituent transcripts (28).

Single-nucleus RNA-seq analysis

For striatum samples, the 10X Genomics *Cell Ranger* v7.2.0 (67) pipeline was used to align reads from snRNA-seq to a version of the mouse mm10 reference transcriptome that includes introns (refdata-gex-mm10-2020-A, 10X Genomics). The –chemistry=SC3Pv3 and –include-introns=TRUE flags were used in addition to default parameters for Cell Ranger count. For PFC samples, Cell Ranger v3.0.2 was used with the same reference transcriptome. Ambient RNA removal was performed on striatum samples using CellBender v0.3.0 (68). Unique Molecular Identifier (UMI) counts were analyzed using the *Seurat* v4.4.0 package (69). Nuclei expressing less than 500 genes were removed and the remaining nuclei were normalized by total expression, multiplied by ten thousand, and log transformed. Seurat's *ScaleData* function was then used to scale the data. Linear dimension reduction by PCA was performed using Seurat's RunPCA function on the scaled data on variable genes, and significant PCs were identified. The nuclei were clustered in the PCA space using Seurat's FindNeighbors and FindClusters functions then visualized using Uniform Manifold Approximation and Projection (UMAP) using significant PCs. Doublet identification was performed using the *Scrublet* v0.2.3 Python package (70) with default parameters. Clusters and nuclei with a scrublet score above the region-specific thresholds (0.40 for 1-month PFC and 0.41 for 1-month striatum) were determined to be doublets and were removed from the data.

UMAP clusters were assigned to cell type by manual examination of enrichment/depletion of brain-region-specific cell type marker genes. Neuronal subtypes were identified by re-clustering the nuclei of a major cell type and evaluating expression of subtype-specific marker genes. Marker genes were obtained from dropviz.org (22).

Cell composition analysis

Cell composition analysis was performed in R using the *speckle* v1.0.0 (71). The *propeller* function with *arcsin* normalization was used to test for statistical differences in major cell type and subtype composition between genotypes in each examined brain region. For striatum samples, cell composition analysis was performed using either inhibitory neurons as a whole or after dividing inhibitory neurons into subtypes (dSPN, iSPN, eSPN, PV interneurons).

Single-nucleus RNA-seq DE

DE analysis (*Srrm2*$^{+/-}$ vs. WT) was performed using the scOnline pseudocell method (72, 73) for each cell type and subtype in each brain region. By aggregating the expression of a group of nuclei with similar transcriptomes within each replicate, cell type, and subtype, this method resolves known technical variation issues of snRNA-seq transcriptome data including low capture rates from dropouts and pseudoreplication, while avoiding the pitfalls of pseudobulk approaches, such as low statistical power and high variation in sample sizes (72, 73). To construct pseudocells, single nuclei were grouped by cell type for each sample. Within each group, pseudocell centers were identified by applying k-means clustering so that each cluster contained 20 nuclei at minimum and 40 nuclei on average. Cell types and subtypes that were identified but did not have enough nuclei present to create at least two pseudocells per sample were removed. To generate the pseudocell counts matrix, we aggregated the raw UMI counts of cells assigned to each pseudocell. Differential expression analysis was performed using limma's *duplicateCorrelation* mixed model analysis function with robust empirical Bayes moderated

t-statistics and mouse ID as random effect. Genotype and the percentage of mitochondrial reads were used as covariates for all analyses. Genes with FDR-adjusted *P*-value of < 0.01 were defined as DE genes.

Proteomics data analysis

Mass spectra were analyzed using Spectrum Mill MS Proteomics Software (Broad Institute) with a mouse database from Uniprot.org downloaded on 04/07/2021 containing 55734 entries. Search parameters included: ESI Q Exactive HCD v4-35-20 scoring, parent and fragment mass tolerance of 20 ppm, 40% minimum matched peak intensity, trypsin allow P enzyme specificity with up to four missed cleavages, and calculate reversed database scores enabled. Fixed modifications were carbamidomethylation at cysteine. TMT labeling was required at lysine, but peptide N termini could be labeled or unlabeled. Allowed variable modifications were protein N-terminal acetylation, oxidized methionine, pyroglutamic acid, and pyro carbamidomethyl cysteine. Protein quantification was achieved by taking the ratio of TMT reporter ions for each sample over the TMT reporter ion for the median of all channels. TMT18 reporter ion intensities were corrected for isotopic impurities in the Spectrum Mill protein/peptide summary module using the afRICA correction method which implements determinant calculations according to Cramer's Rule and correction factors obtained from the reagent manufacturer's certificate of analysis (https://www.thermofisher.com/order/catalog/product/90406) for lot numbers VH310017 and WG333575. After performing median normalization, a moderated two-sample t-test was applied to the datasets to compare WT and *Srrm2*$^{+/-}$ sample groups at 1- and 4-months of age.

Gene set enrichment analysis

GSEA was performed with the R Bioconductor package *fgsea* (74). Genes/proteins were pre-ranked using the appropriate test-statistics (DESeq2 Wald test-statistic for bulk RNA-seq, and the moderated t-test statistic for single-nucleus RNA-seq and synapse proteomics experiments). We carried out GSEA using two independent gene set collections—M5 ontology gene sets (v2023.2) obtained from the Molecular signatures database (MSigDB) (17), and (ii) SynGO gene sets (v1.2) (18) combined with other curated gene sets, which include SCZ GWAS hits (20), SFARI ASD risk genes (75), bipolar GWAS hits (19). Also combined with SynGO sets were the 'activity regulated' gene-set, which consisted of neuronal activity-induced rapid, delayed and slow primary response genes defined by Tyssowski et al. (76), and the 'dopamine-induced' gene-set, consisting of genes with FDR-adjusted *P*-value < 0.1 that were upregulated in striatal neuronal culture following one hour dopamine treatment (77). For proteins with multiple isoforms, the isoform with the largest effect-size was used for pre-ranking. Because the enrichment analyses were carried out using the proteins' gene symbols, we use the terms gene set and protein set interchangeably in this study.

EEG data analysis

All raw recordings were segmented into 10-second epochs, and each epoch was classified into NREM, REM, or wake stages using the Light Gradient Boosting Machine (LightGBM) algorithm, as previously described (39). Sleep spindle detection was performed using the Luna toolbox, which uses a wavelet-based detection method (78). Spindle density, amplitude, integrated spindle activity (ISA), and spindle duration were calculated for all animals based on the detection threshold of WT animals. Spindle parameters and power density data

were then analyzed using a linear mixed-effects model (ex. *spindle density ~ genotype* frequency + subjectID*) performed in Python. The statistical impact of genotype on measures was based on likelihood ratio test between two models: (*spindle density ~ genotype* frequency + subjectID*) and (*spindle density ~ frequency + subjectID*). Prior to statistical analysis, spindle density outliers were removed using stringent 2IQR (interquartile range method), where values below Q1 - 2IQR or above Q3 + 2IQR were considered outliers. For each subject and genotype group (WT, *Srrm2*$^{+/-}$), spindle parameters and EEG power were averaged across conditions and grouped by subject ID, genotype, and frequency band (F). Spindle detection was performed using different center frequencies (9, 11, 13, 15 Hz). For EEG power analysis, we examined different frequency bands, including slow oscillations, delta, theta, alpha, sigma, beta, and gamma bands. The statistical significance of differences across genotypes and frequency bands was evaluated using *P*-values from the mixed model output, with a significance threshold set at $P < 0.05$.

Resource Availability

Supplementary tables are available at https://doi.org/10.5281/zenodo.13910034. The original mass spectra and the protein sequence database used for searches have been deposited in the public proteomics repository MassIVE (http://massive.ucsd.edu) and are accessible at ftp://MSV000095963@massive.ucsd.edu. Raw bulk and single nucleus RNA sequencing fastqs are being deposited at NCBI GEO. All datasets will be made public upon acceptance of the manuscript.

References

1. D. Vigo, G. Thornicroft, R. Atun, Estimating the true global burden of mental illness. *The Lancet Psychiatry* **3**, 171–178 (2016).
2. T. Singh, *et al.*, Rare coding variants in ten genes confer substantial risk for schizophrenia. *Nature* **604**, 509–516 (2022).
3. D. Liu, *et al.*, Schizophrenia risk conferred by rare protein-truncating variants is conserved across diverse human populations. *Nat Genet* **55**, 369–376 (2023).
4. J. Kaplanis, *et al.*, Evidence for 28 genetic disorders discovered by combining healthcare and research data. *Nature* **586**, 757–762 (2020).
5. S. Cuinat, *et al.*, Loss-of-function variants in SRRM2 cause a neurodevelopmental disorder. *Genetics in Medicine* **24**, 1774–1780 (2022).
6. B. J. Blencowe, R. Issner, J. A. Nickerson, P. A. Sharp, A coactivator of pre-mRNA splicing. *Genes Dev* **12**, 996–1009 (1998).
7. B. J. Blencowe, *et al.*, The SRm160/300 splicing coactivator subunits. *RNA* **6**, 111–120 (2000).
8. S. Xu, *et al.*, SRRM2 organizes splicing condensates to regulate alternative splicing. *Nucleic Acids Res* **50**, 8599–8614 (2022).
9. M. Khanna, *et al.*, A systematic characterization of Cwc21, the yeast ortholog of the human spliceosomal protein SRm300. *RNA* **15**, 2174 (2009).
10. İ. A. Ilik, *et al.*, SON and SRRM2 are essential for nuclear speckle formation. *eLife* **9**, e60579 (2020).
11. D. L. Spector, A. I. Lamond, Nuclear Speckles. *Cold Spring Harb Perspect Biol* **3**, a000646

(2011).
12. M. J. Gandal, *et al.*, Transcriptome-wide isoform-level dysregulation in ASD, schizophrenia, and bipolar disorder. *Science* **362**, eaat8127 (2018).
13. S. H. Ahanger, *et al.*, Distinct nuclear compartment-associated genome architecture in the developing mammalian brain. *Nat Neurosci* **24**, 1235–1242 (2021).
14. T. Groza, *et al.*, The International Mouse Phenotyping Consortium: comprehensive knockout phenotyping underpinning the study of human disease. *Nucleic Acids Research* **51**, D1038–D1045 (2023).
15. M.-F. Xiao, *et al.*, A biomarker-authenticated model of schizophrenia implicating NPTX2 loss of function. *Science Advances* **7**, eabf6935 (2021).
16. S. Aryal, *et al.*, Deep proteomics identifies shared molecular pathway alterations in synapses of patients with schizophrenia and bipolar disorder and mouse model. *Cell Reports* **42** (2023).
17. A. S. Castanza, *et al.*, Extending support for mouse data in the Molecular Signatures Database (MSigDB). *Nat Methods* **20**, 1619–1620 (2023).
18. F. Koopmans, *et al.*, SynGO: An Evidence-Based, Expert-Curated Knowledge Base for the Synapse. *Neuron* **103**, 217-234.e4 (2019).
19. N. Mullins, *et al.*, Genome-wide association study of more than 40,000 bipolar disorder cases provides new insights into the underlying biology. *Nat Genet* **53**, 817–829 (2021).
20. V. Trubetskoy, *et al.*, Mapping genomic loci implicates genes and synaptic biology in schizophrenia. *Nature* **604**, 502–508 (2022).
21. R. A. McCutcheon, J. H. Krystal, O. D. Howes, Dopamine and glutamate in schizophrenia: biology, symptoms and treatment. *World Psychiatry* **19**, 15–33 (2020).
22. A. Saunders, *et al.*, Molecular Diversity and Specializations among the Cells of the Adult Mouse Brain. *Cell* **174**, 1015-1030.e16 (2018).
23. B. Wilkinson, J. Li, M. P. Coba, Synaptic GAP and GEF Complexes Cluster Proteins Essential for GTP Signaling. *Sci Rep* **7**, 5272 (2017).
24. D. R. M. Vlaskamp, *et al.*, SYNGAP1 encephalopathy. *Neurology* **92**, e96–e107 (2019).
25. Y. Araki, *et al.*, SynGAP isoforms differentially regulate synaptic plasticity and dendritic development. *eLife* **9**, e56273 (2020).
26. G. Gou, *et al.*, SynGAP splice variants display heterogeneous spatio-temporal expression and subcellular distribution in the developing mammalian brain. *Journal of Neurochemistry* **154**, 618–634 (2020).
27. Y. Oku, R. L. Huganir, AGAP3 and Arf6 Regulate Trafficking of AMPA Receptors and Synaptic Plasticity. *J. Neurosci.* **33**, 12586–12598 (2013).
28. L. Yi, H. Pimentel, N. L. Bray, L. Pachter, Gene-level differential analysis at transcript-level resolution. *Genome Biology* **19**, 53 (2018).
29. F. J. Raabe, *et al.*, Oligodendrocytes as A New Therapeutic Target in Schizophrenia: From Histopathological Findings to Neuron-Oligodendrocyte Interaction. *Cells* **8**, 1496 (2019).
30. A. A. Grace, Dysregulation of the dopamine system in the pathophysiology of schizophrenia and depression. *Nat Rev Neurosci* **17**, 524–532 (2016).
31. J. Peng, *et al.*, Semiquantitative Proteomic Analysis of Rat Forebrain Postsynaptic Density Fractions by Mass Spectrometry. *J. Biol. Chem.* **279**, 21003–21011 (2004).
32. Z. Yao, *et al.*, A taxonomy of transcriptomic cell types across the isocortex and hippocampal

formation. *Cell* **184**, 3222-3241.e26 (2021).
33. L. Darbelli, K. Choquet, S. Richard, C. L. Kleinman, Transcriptome profiling of mouse brains with qkI-deficient oligodendrocytes reveals major alternative splicing defects including self-splicing. *Sci Rep* **7**, 7554 (2017).
34. J. M. Bin, S. N. Harris, T. E. Kennedy, The oligodendrocyte-specific antibody "CC1" binds Quaking 7. *J Neurochem* **139**, 181–186 (2016).
35. E. Ling, *et al.*, A concerted neuron–astrocyte program declines in ageing and schizophrenia. *Nature* **627**, 604–611 (2024).
36. N. Kozhemiako, *et al.*, Non-rapid eye movement sleep and wake neurophysiology in schizophrenia. *eLife* **11**, e76211 (2022).
37. N. Kozhemiako, *et al.*, A spectrum of altered non-rapid eye movement sleep in schizophrenia. [Preprint] (2023). Available at: https://www.biorxiv.org/content/10.1101/2023.12.28.573548v1 [Accessed 5 August 2024].
38. L. E. Herzog, *et al.*, Mouse mutants in schizophrenia risk genes GRIN2A and AKAP11 show EEG abnormalities in common with schizophrenia patients. [Preprint] (2022). Available at: https://www.biorxiv.org/content/10.1101/2022.04.05.487037v1 [Accessed 26 August 2022].
39. L. A. Wang, R. Kern, E. Yu, S. Choi, J. Q. Pan, IntelliSleepScorer, a software package with a graphic user interface for automated sleep stage scoring in mice based on a light gradient boosting machine algorithm. *Sci Rep* **13**, 4275 (2023).
40. J. W. Hofmann, W. W. Seeley, E. J. Huang, RNA Binding Proteins and the Pathogenesis of Frontotemporal Lobar Degeneration. *Annu Rev Pathol* **14**, 469–495 (2019).
41. M. L. Waldö, L. Gustafson, U. Passant, E. Englund, Psychotic symptoms in frontotemporal dementia: a diagnostic dilemma? *International Psychogeriatrics / Ipa* **27**, 531 (2015).
42. N. Y. Tse, *et al.*, Schizotypal traits across the amyotrophic lateral sclerosis–frontotemporal dementia spectrum: pathomechanistic insights. *J Neurol* **269**, 4241–4252 (2022).
43. E. Lester, *et al.*, Tau aggregates are RNA-protein assemblies that mislocalize multiple nuclear speckle components. *Neuron* **0** (2021).
44. R. Wu, *et al.*, Disruption of nuclear speckle integrity dysregulates RNA splicing in C9ORF72-FTD/ALS. *Neuron* (2024). https://doi.org/10.1016/j.neuron.2024.07.025.
45. Z. Farsi, *et al.*, Brain-region-specific changes in neurons and glia and dysregulation of dopamine signaling in Grin2a mutant mice. *Neuron* (2023). https://doi.org/10.1016/j.neuron.2023.08.004.
46. W. S. Stone, *et al.*, Neurodegenerative model of schizophrenia: Growing evidence to support a revisit. *Schizophrenia Research* **243**, 154–162 (2022).
47. M. J. Minzenberg, A. R. Laird, S. Thelen, C. S. Carter, D. C. Glahn, Meta-analysis of 41 Functional Neuroimaging Studies of Executive Function in Schizophrenia. *Archives of General Psychiatry* **66**, 811–822 (2009).
48. J. R. Tregellas, *et al.*, Intrinsic Hippocampal Activity as a Biomarker for Cognition and Symptoms in Schizophrenia. *AJP* **171**, 549–556 (2014).
49. M. Laruelle, A. Abi-Dargham, Dopamine as the wind of the psychotic fire: new evidence from brain imaging studies. *J Psychopharmacol* **13**, 358–371 (1999).
50. A. E. Jaffe, *et al.*, Developmental and genetic regulation of the human cortex transcriptome

illuminate schizophrenia pathogenesis. *Nat Neurosci* **21**, 1117–1125 (2018).
51. Y. Araki, *et al.*, SynGAP regulates synaptic plasticity and cognition independently of its catalytic activity. *Science* **383**, eadk1291 (2024).
52. M. Zeng, G. Bai, M. Zhang, Anchoring high concentrations of SynGAP at postsynaptic densities via liquid-liquid phase separation. *Small GTPases* **10**, 296–304 (2017).
53. X. Wang, Y. Wang, Q. Cai, M. Zhang, AIDA-1/ANKS1B Binds to the SynGAP Family RasGAPs with High Affinity and Specificity. *Journal of Molecular Biology* **436**, 168608 (2024).
54. T. R. Gamache, Y. Araki, R. L. Huganir, Twenty Years of SynGAP Research: From Synapses to Cognition. *J. Neurosci.* **40**, 1596–1605 (2020).
55. M. Valdés-Tovar, *et al.*, Insights into myelin dysfunction in schizophrenia and bipolar disorder. *World J Psychiatry* **12**, 264–285 (2022).
56. H. Mathys, *et al.*, Single-cell transcriptomic analysis of Alzheimer's disease. *Nature* **570**, 332–337 (2019).
57. C. Depp, *et al.*, Myelin dysfunction drives amyloid-β deposition in models of Alzheimer's disease. *Nature* **618**, 349–357 (2023).
58. S. Kelly, *et al.*, Widespread white matter microstructural differences in schizophrenia across 4322 individuals: results from the ENIGMA Schizophrenia DTI Working Group. *Mol Psychiatry* **23**, 1261–1269 (2018).
59. C. X. Yap, *et al.*, Brain cell-type shifts in Alzheimer's disease, autism, and schizophrenia interrogated using methylomics and genetics. *Science Advances* **10**, eadn7655 (2024).
60. K. J. Karczewski, *et al.*, Systematic single-variant and gene-based association testing of thousands of phenotypes in 394,841 UK Biobank exomes. *Cell Genomics* **2** (2022).
61. C. Vanderburg, *et al.*, Fresh Frozen Mouse Brain Preparation (for Single Nuclei Sequencing). (2020).
62. C. Martin, *et al.*, Frozen Tissue Nuclei Extraction. (2020).
63. B. Li, C. N. Dewey, RSEM: accurate transcript quantification from RNA-Seq data with or without a reference genome. *BMC Bioinformatics* **12**, 323 (2011).
64. M. I. Love, W. Huber, S. Anders, Moderated estimation of fold change and dispersion for RNA-seq data with DESeq2. *Genome Biology* **15**, 550 (2014).
65. N. L. Bray, H. Pimentel, P. Melsted, L. Pachter, Near-optimal probabilistic RNA-seq quantification. *Nat Biotechnol* **34**, 525–527 (2016).
66. H. Pimentel, N. L. Bray, S. Puente, P. Melsted, L. Pachter, Differential analysis of RNA-seq incorporating quantification uncertainty. *Nat Methods* **14**, 687–690 (2017).
67. G. X. Y. Zheng, *et al.*, Massively parallel digital transcriptional profiling of single cells. *Nat Commun* **8**, 14049 (2017).
68. S. J. Fleming, *et al.*, Unsupervised removal of systematic background noise from droplet-based single-cell experiments using CellBender. *Nat Methods* **20**, 1323–1335 (2023).
69. T. Stuart, *et al.*, Comprehensive Integration of Single-Cell Data. *Cell* **177**, 1888-1902.e21 (2019).
70. S. L. Wolock, R. Lopez, A. M. Klein, Scrublet: Computational Identification of Cell Doublets in Single-Cell Transcriptomic Data. *cels* **8**, 281-291.e9 (2019).
71. B. Phipson, *et al.*, propeller: testing for differences in cell type proportions in single cell data. *Bioinformatics* **38**, 4720–4726 (2022).

72. J. Langlieb, *et al.*, The molecular cytoarchitecture of the adult mouse brain. *Nature* **624**, 333–342 (2023).
73. V. Gazestani, *et al.*, Early Alzheimer's disease pathology in human cortex involves transient cell states. *Cell* **186**, 4438-4453.e23 (2023).
74. G. Korotkevich, *et al.*, Fast gene set enrichment analysis. [Preprint] (2021). Available at: https://www.biorxiv.org/content/10.1101/060012v3 [Accessed 9 September 2024].
75. B. S. Abrahams, *et al.*, SFARI Gene 2.0: a community-driven knowledgebase for the autism spectrum disorders (ASDs). *Mol Autism* **4**, 36 (2013).
76. K. M. Tyssowski, *et al.*, Different neuronal activity patterns induce different gene expression programs. *Neuron* **98**, 530-546.e11 (2018).
77. K. E. Savell, *et al.*, A dopamine-induced gene expression signature regulates neuronal function and cocaine response. *Science Advances* **6**, eaba4221 (2020).
78. A. Ghoshal, *et al.*, Effects of a patient-derived de novo coding alteration of CACNA1I in mice connect a schizophrenia risk gene with sleep spindle deficits. *Transl Psychiatry* **10**, 29 (2020).

Fig. 1

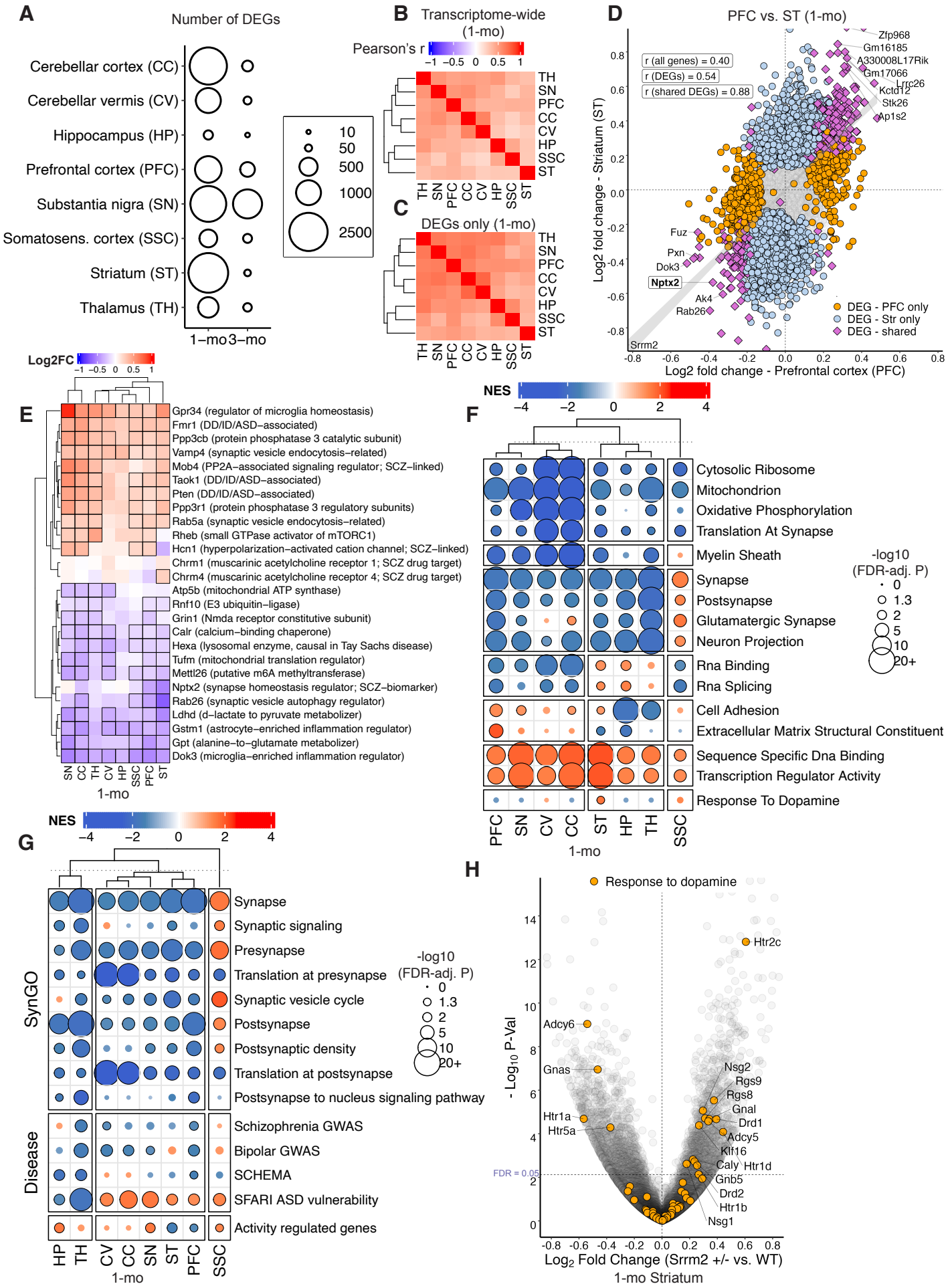
A
Number of DEGs
Cerebellar cortex (CC)
Cerebellar vermis (CV)
Hippocampus (HP)
Prefrontal cortex (PFC)
Substantia nigra (SN)
Somatosens. cortex (SSC)
Striatum (ST)
Thalamus (TH)
1–mo
3–mo
10
50
500
1000
2500
B
Transcriptome-wide (1-mo)
Pearson's r
−1 −0.5 0 0.5 1
TH SN PFC CC CV HP SSC ST
C
DEGs only (1-mo)
D
PFC vs. ST (1-mo)
r (all genes) = 0.40
r (DEGs) = 0.54
r (shared DEGs) = 0.88
Zfp968
Gm16185
A330008L17Rik
Gm17066
Lrrc26
Kctd12
Stk26
Ap1s2
Fuz
Pxn
Dok3
Nptx2
Ak4
Rab26
Srrm2
DEG - PFC only
DEG - Str only
DEG - shared
Log2 fold change - Striatum (ST)
Log2 fold change - Prefrontal cortex (PFC)
E
Log2FC
−1 −0.5 0 0.5 1
Gpr34 (regulator of microglia homeostasis)
Fmr1 (DD/ID/ASD–associated)
Ppp3cb (protein phosphatase 3 catalytic subunit)
Vamp4 (synaptic vesicle endocytosis–related)
Mob4 (PP2A–associated signaling regulator; SCZ–linked)
Taok1 (DD/ID/ASD–associated)
Pten (DD/ID/ASD–associated)
Ppp3r1 (protein phosphatase 3 regulatory subunits)
Rab5a (synaptic vesicle endocytosis–related)
Rheb (small GTPase activator of mTORC1)
Hcn1 (hyperpolarization–activated cation channel; SCZ–linked)
Chrm1 (muscarinic acetylcholine receptor 1; SCZ drug target)
Chrm4 (muscarinic acetylcholine receptor 4; SCZ drug target)
Atp5b (mitochondrial ATP synthase)
Rnf10 (E3 ubiquitin–ligase)
Grin1 (Nmda receptor constitutive subunit)
Calr (calcium–binding chaperone)
Hexa (lysosomal enzyme, causal in Tay Sachs disease)
Tufm (mitochondrial translation regulator)
Mettl26 (putative m6A methyltransferase)
Nptx2 (synapse homeostasis regulator; SCZ–biomarker)
Rab26 (synaptic vesicle autophagy regulator)
Ldhd (d–lactate to pyruvate metabolizer)
Gstm1 (astrocyte–enriched inflammation regulator)
Gpt (alanine–to–glutamate metabolizer)
Dok3 (microglia–enriched inflammation regulator)
SN CC TH CV HP SSC PFC ST
1-mo
F
NES
−4 −2 0 2 4
Cytosolic Ribosome
Mitochondrion
Oxidative Phosphorylation
Translation At Synapse
Myelin Sheath
Synapse
Postsynapse
Glutamatergic Synapse
Neuron Projection
Rna Binding
Rna Splicing
Cell Adhesion
Extracellular Matrix Structural Constituent
Sequence Specific Dna Binding
Transcription Regulator Activity
Response To Dopamine
-log10 (FDR-adj. P)
0
1.3
2
5
10
20+
PFC SN CV CC ST HP TH SSC
1-mo
G
NES
−4 −2 0 2 4
SynGO
Synapse
Synaptic signaling
Presynapse
Translation at presynapse
Synaptic vesicle cycle
Postsynapse
Postsynaptic density
Translation at postsynapse
Postsynapse to nucleus signaling pathway
Disease
Schizophrenia GWAS
Bipolar GWAS
SCHEMA
SFARI ASD vulnerability
Activity regulated genes
-log10 (FDR-adj. P)
0
1.3
2
5
10
20+
HP TH CV CC SN ST PFC SSC
1-mo
H
Response to dopamine
Htr2c
Adcy6
Gnas
Htr1a
Htr5a
Nsg2
Rgs9
Rgs8
Gnal
Drd1
Adcy5
Klf16
Caly
Htr1d
Gnb5
Drd2
Htr1b
Nsg1
FDR = 0.05
- Log10 P-Val
Log2 Fold Change (Srrm2 +/- vs. WT)
1-mo Striatum

Fig. 2

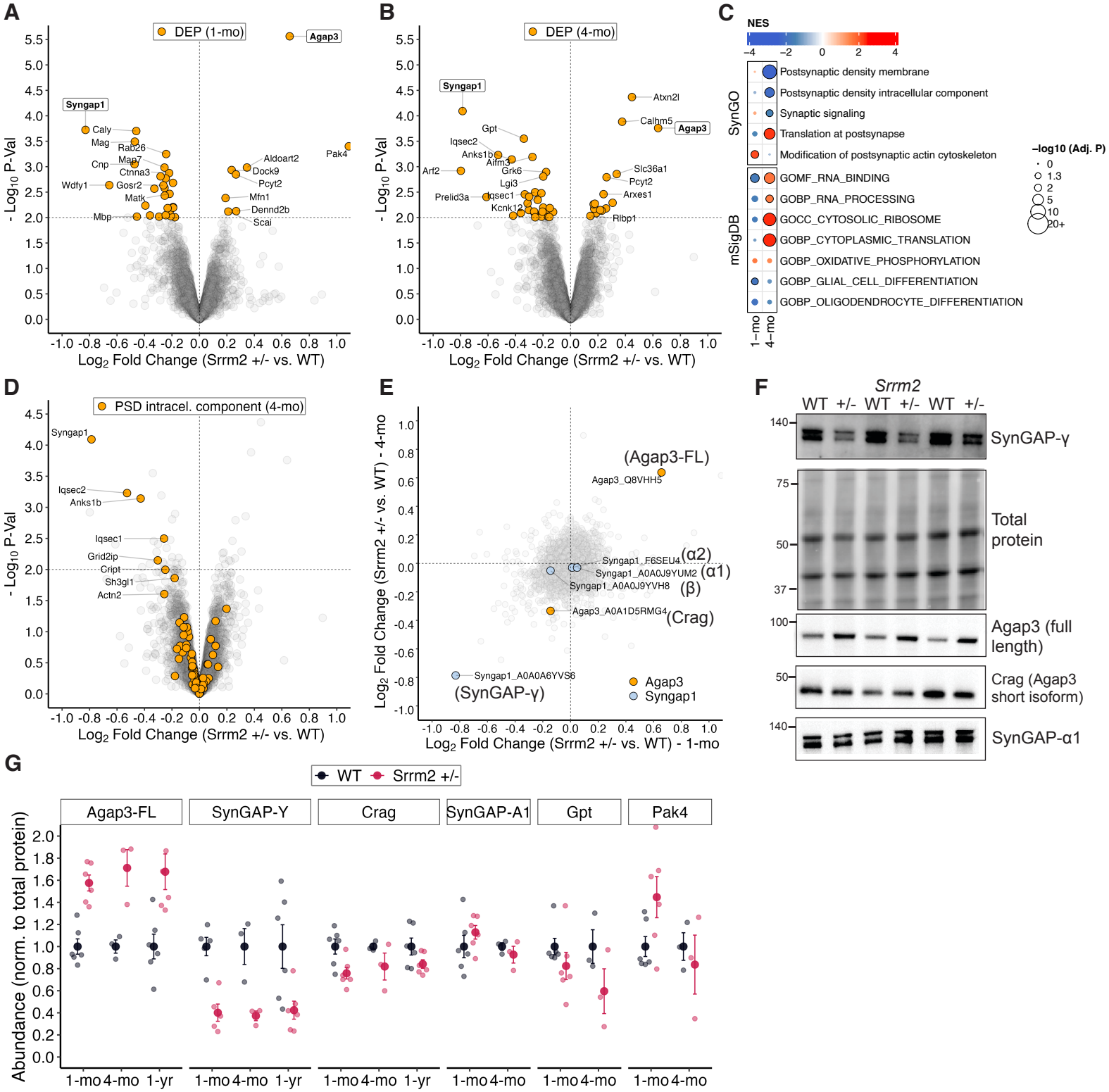
A
DEP (1-mo)
Agap3
Syngap1
Caly
Mag
Rab26
Map7
Cnp
Ctnna3
Wdfy1
Gosr2
Matk
Mbp
Aldoart2
Dock9
Pcyt2
Mfn1
Dennd2b
Scai
Pak4
- Log10 P-Val
Log2 Fold Change (Srrm2 +/- vs. WT)
B
DEP (4-mo)
Syngap1
Atxn2l
Calhm5
Agap3
Gpt
Iqsec2
Anks1b
Aifm3
Grk6
Arf2
Lgi3
Prelid3a
Iqsec1
Kcnk12
Slc36a1
Pcyt2
Arxes1
Rlbp1
- Log10 P-Val
Log2 Fold Change (Srrm2 +/- vs. WT)
C
NES
−4 −2 0 2 4
SynGO
Postsynaptic density membrane
Postsynaptic density intracellular component
Synaptic signaling
Translation at postsynapse
Modification of postsynaptic actin cytoskeleton
mSigDB
GOMF_RNA_BINDING
GOBP_RNA_PROCESSING
GOCC_CYTOSOLIC_RIBOSOME
GOBP_CYTOPLASMIC_TRANSLATION
GOBP_OXIDATIVE_PHOSPHORYLATION
GOBP_GLIAL_CELL_DIFFERENTIATION
GOBP_OLIGODENDROCYTE_DIFFERENTIATION
1−mo
4−mo
−log10 (Adj. P)
0
1.3
2
5
10
20+
D
PSD intracel. component (4-mo)
Syngap1
Iqsec2
Anks1b
Iqsec1
Grid2ip
Cript
Sh3gl1
Actn2
- Log10 P-Val
Log2 Fold Change (Srrm2 +/- vs. WT)
E
(Agap3-FL)
Agap3_Q8VHH5
Syngap1_F6SEU4
(α2)
Syngap1_A0A0J9YUM2
(α1)
Syngap1_A0A0J9YVH8
(β)
Agap3_A0A1D5RMG4
(Crag)
Syngap1_A0A0A6YVS6
(SynGAP-γ)
Agap3
Syngap1
Log2 Fold Change (Srrm2 +/- vs. WT) - 4-mo
Log2 Fold Change (Srrm2 +/- vs. WT) - 1-mo
F
Srrm2
WT +/- WT +/- WT +/-
140
SynGAP-γ
75
50
37
Total protein
100
Agap3 (full length)
50
Crag (Agap3 short isoform)
140
SynGAP-α1
G
WT
Srrm2 +/-
Agap3-FL
SynGAP-Y
Crag
SynGAP-A1
Gpt
Pak4
Abundance (norm. to total protein)
1-mo 4-mo 1-yr

Fig. 3

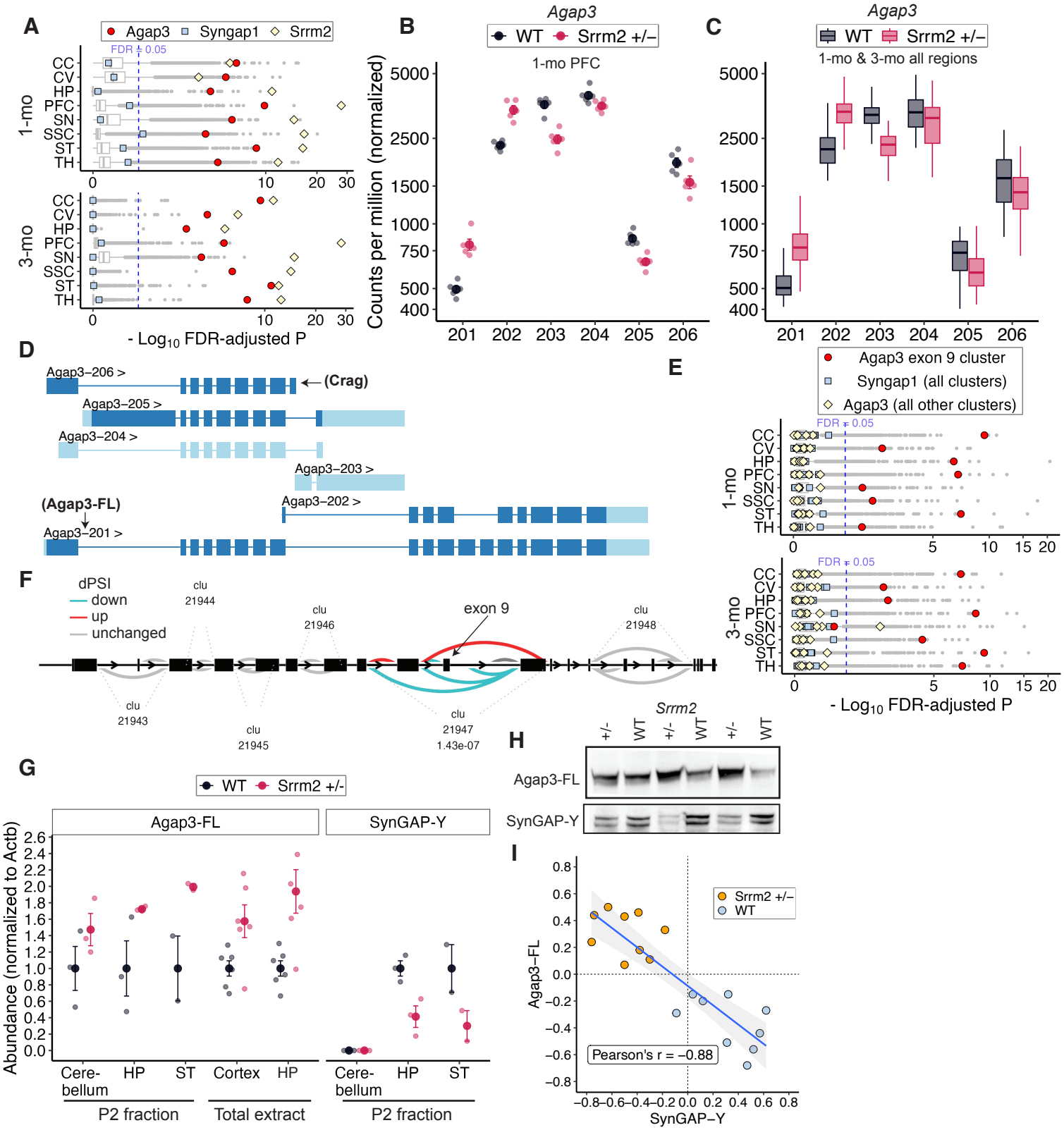
A
Agap3
Syngap1
Srrm2
FDR = 0.05
1-mo
3-mo
CC
CV
HP
PFC
SN
SSC
ST
TH
- Log10 FDR-adjusted P
B
Agap3
WT
Srrm2 +/–
1-mo PFC
Counts per million (normalized)
C
Agap3
WT
Srrm2 +/–
1-mo & 3-mo all regions
D
Agap3–206 >
(Crag)
Agap3–205 >
Agap3–204 >
Agap3–203 >
(Agap3-FL)
Agap3–202 >
Agap3–201 >
E
Agap3 exon 9 cluster
Syngap1 (all clusters)
Agap3 (all other clusters)
FDR = 0.05
1-mo
3-mo
- Log10 FDR-adjusted P
F
dPSI
down
up
unchanged
clu 21944
clu 21946
exon 9
clu 21948
clu 21943
clu 21945
clu 21947
1.43e-07
G
WT
Srrm2 +/-
Agap3-FL
SynGAP-Y
Abundance (normalized to Actb)
Cere-bellum
HP
ST
Cortex
HP
Cere-bellum
HP
ST
P2 fraction
Total extract
P2 fraction
H
Srrm2
+/-
WT
+/-
WT
+/-
WT
Agap3-FL
SynGAP-Y
I
Srrm2 +/–
WT
Agap3–FL
SynGAP–Y
Pearson's r = –0.88

Fig. 4

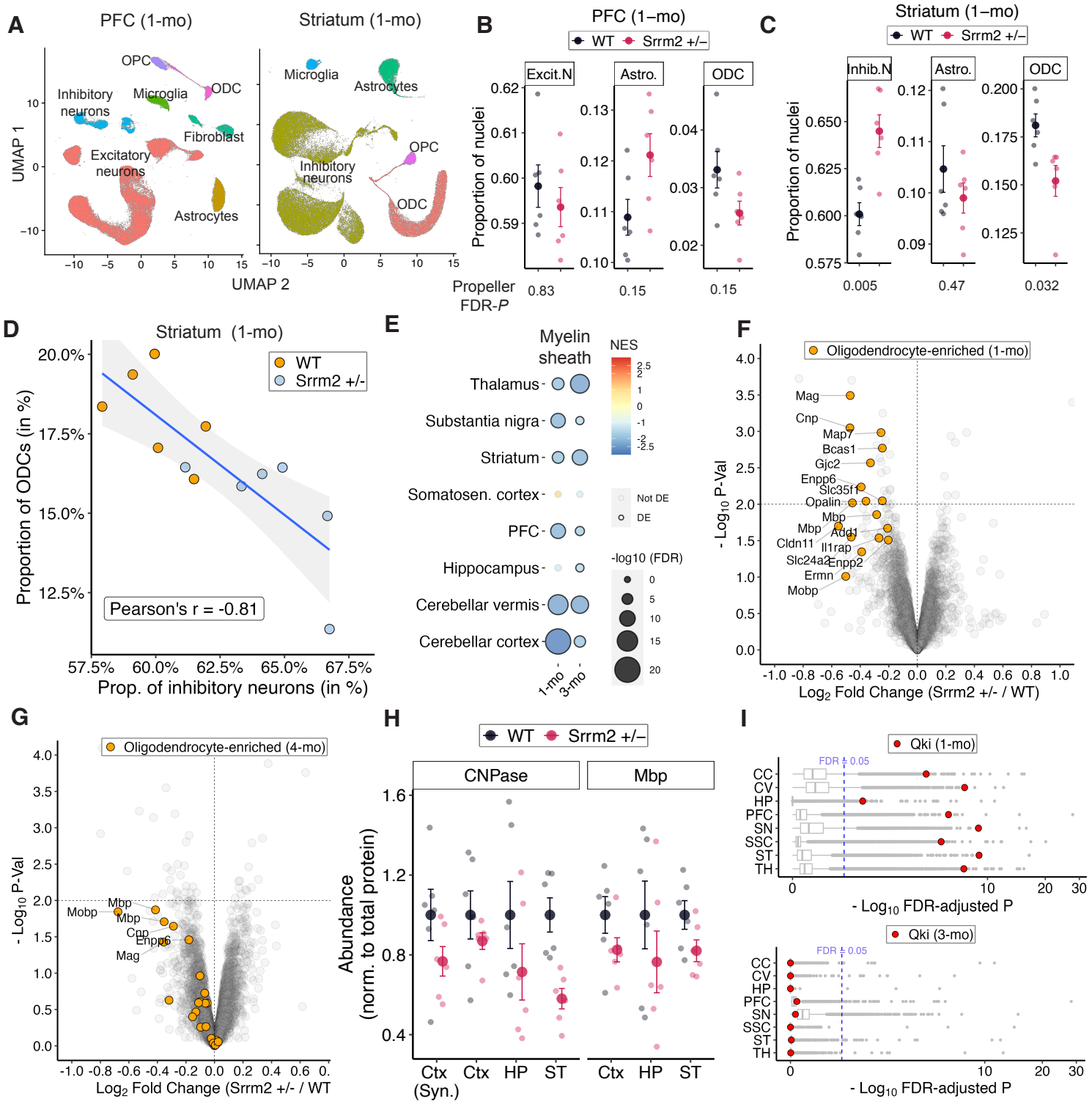
A
PFC (1-mo)
Striatum (1-mo)
OPC
Inhibitory neurons
Microglia
ODC
Fibroblast
Excitatory neurons
Astrocytes
UMAP 1
UMAP 2
B
PFC (1–mo)
WT
Srrm2 +/–
Excit.N
Astro.
ODC
Proportion of nuclei
Propeller FDR-P
0.83
0.15
0.15
C
Striatum (1–mo)
Inhib.N
Astro.
ODC
0.005
0.47
0.032
D
Striatum (1-mo)
WT
Srrm2 +/-
Proportion of ODCs (in %)
Pearson's r = -0.81
Prop. of inhibitory neurons (in %)
E
Myelin sheath
NES
Thalamus
Substantia nigra
Striatum
Somatosen. cortex
PFC
Hippocampus
Cerebellar vermis
Cerebellar cortex
1-mo
3-mo
Not DE
DE
-log10 (FDR)
F
Oligodendrocyte-enriched (1-mo)
Mag
Cnp
Map7
Bcas1
Gjc2
Enpp6
Slc35f1
Opalin
Mbp
Add1
Cldn11
Il1rap
Slc24a2
Enpp2
Ermn
Mobp
- Log10 P-Val
Log2 Fold Change (Srrm2 +/- / WT)
G
Oligodendrocyte-enriched (4-mo)
Mobp
Mbp
Cnp
Enpp6
Mag
- Log10 P-Val
Log2 Fold Change (Srrm2 +/- / WT
H
WT
Srrm2 +/–
CNPase
Mbp
Abundance (norm. to total protein)
Ctx (Syn.)
Ctx
HP
ST
Ctx
HP
ST
I
Qki (1-mo)
FDR = 0.05
CC
CV
HP
PFC
SN
SSC
ST
TH
- Log10 FDR-adjusted P
Qki (3-mo)
FDR = 0.05
CC
CV
HP
PFC
SN
SSC
ST
TH
- Log10 FDR-adjusted P

Fig. 5

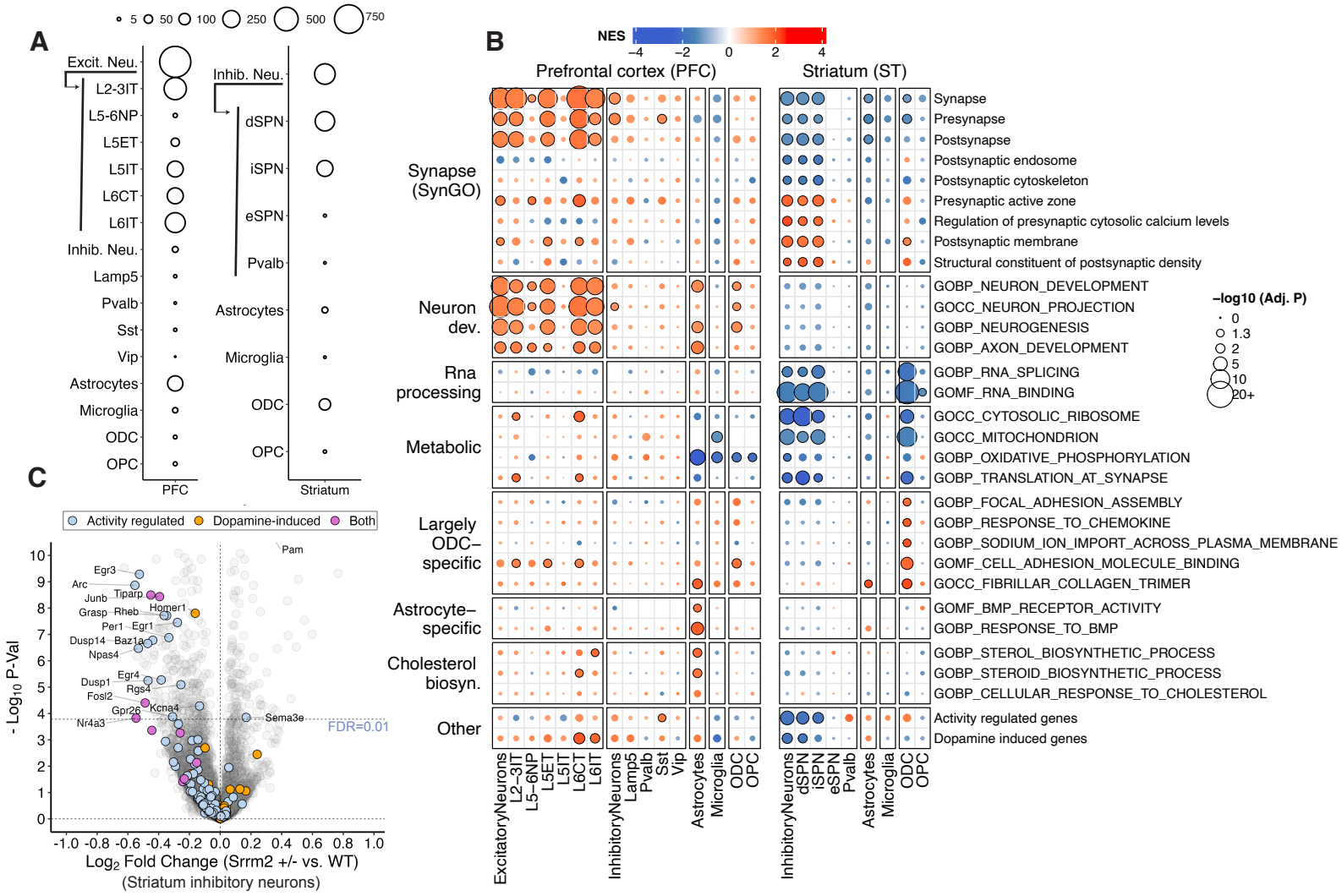
A
5 50 100 250 500 750
Excit. Neu.
L2-3IT
L5-6NP
L5ET
L5IT
L6CT
L6IT
Inhib. Neu.
Lamp5
Pvalb
Sst
Vip
Astrocytes
Microglia
ODC
OPC
PFC
Inhib. Neu.
dSPN
iSPN
eSPN
Pvalb
Astrocytes
Microglia
ODC
OPC
Striatum
B
NES
−4 −2 0 2 4
Prefrontal cortex (PFC)
Striatum (ST)
Synapse (SynGO)
Synapse
Presynapse
Postsynapse
Postsynaptic endosome
Postsynaptic cytoskeleton
Presynaptic active zone
Regulation of presynaptic cytosolic calcium levels
Postsynaptic membrane
Structural constituent of postsynaptic density
Neuron dev.
GOBP_NEURON_DEVELOPMENT
GOCC_NEURON_PROJECTION
GOBP_NEUROGENESIS
GOBP_AXON_DEVELOPMENT
Rna processing
GOBP_RNA_SPLICING
GOMF_RNA_BINDING
Metabolic
GOCC_CYTOSOLIC_RIBOSOME
GOCC_MITOCHONDRION
GOBP_OXIDATIVE_PHOSPHORYLATION
GOBP_TRANSLATION_AT_SYNAPSE
Largely ODC–specific
GOBP_FOCAL_ADHESION_ASSEMBLY
GOBP_RESPONSE_TO_CHEMOKINE
GOBP_SODIUM_ION_IMPORT_ACROSS_PLASMA_MEMBRANE
GOMF_CELL_ADHESION_MOLECULE_BINDING
GOCC_FIBRILLAR_COLLAGEN_TRIMER
Astrocyte–specific
GOMF_BMP_RECEPTOR_ACTIVITY
GOBP_RESPONSE_TO_BMP
Cholesterol biosyn.
GOBP_STEROL_BIOSYNTHETIC_PROCESS
GOBP_STEROID_BIOSYNTHETIC_PROCESS
GOBP_CELLULAR_RESPONSE_TO_CHOLESTEROL
Other
Activity regulated genes
Dopamine induced genes
−log10 (Adj. P)
0
1.3
2
5
10
20+
Excitatory Neurons
L2–3IT
L5–6NP
L5ET
L5IT
L6CT
L6IT
Inhibitory Neurons
Lamp5
Pvalb
Sst
Vip
Astrocytes
Microglia
ODC
OPC
Inhibitory Neurons
dSPN
iSPN
eSPN
Pvalb
Astrocytes
Microglia
ODC
OPC
C
Activity regulated
Dopamine-induced
Both
Pam
Egr3
Arc
Junb
Tiparp
Grasp
Rheb
Homer1
Per1
Egr1
Dusp14
Baz1a
Npas4
Egr4
Dusp1
Rgs4
Fosl2
Gpr26
Kcna4
Nr4a3
Sema3e
FDR=0.01
- Log10 P-Val
Log2 Fold Change (Srrm2 +/- vs. WT)
(Striatum inhibitory neurons)

Fig. 6

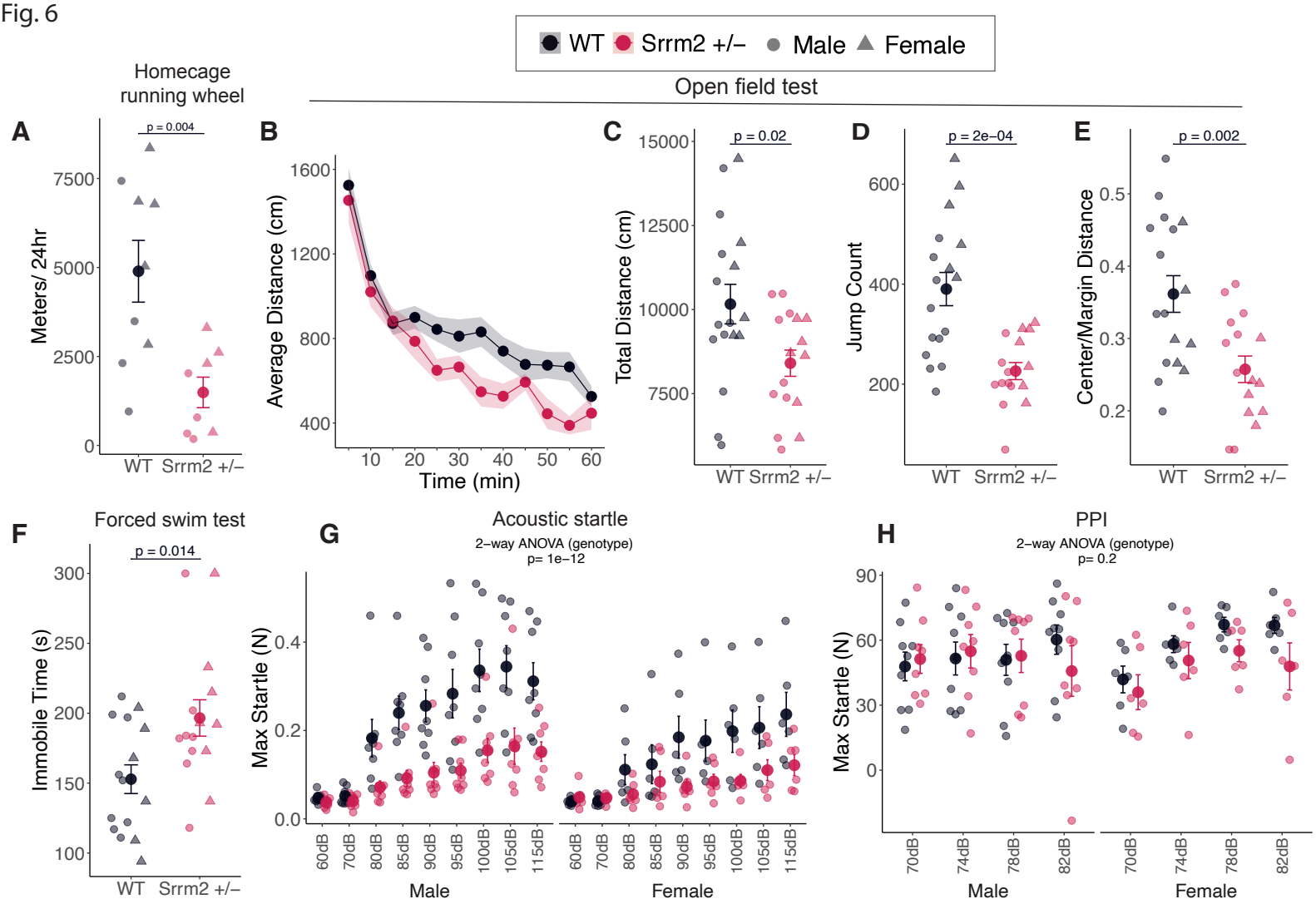
WT
Srrm2 +/−
Male
Female
Homecage running wheel
Open field test
A
p = 0.004
Meters/ 24hr
WT
Srrm2 +/−
B
Average Distance (cm)
Time (min)
C
p = 0.02
Total Distance (cm)
D
p = 2e−04
Jump Count
E
p = 0.002
Center/Margin Distance
F
Forced swim test
p = 0.014
Immobile Time (s)
G
Acoustic startle
2−way ANOVA (genotype)
p= 1e−12
Max Startle (N)
60dB
70dB
80dB
85dB
90dB
95dB
100dB
105dB
115dB
Male
Female
H
PPI
2−way ANOVA (genotype)
p= 0.2
Max Startle (N)
70dB
74dB
78dB
82dB
Male
Female

Fig. 7

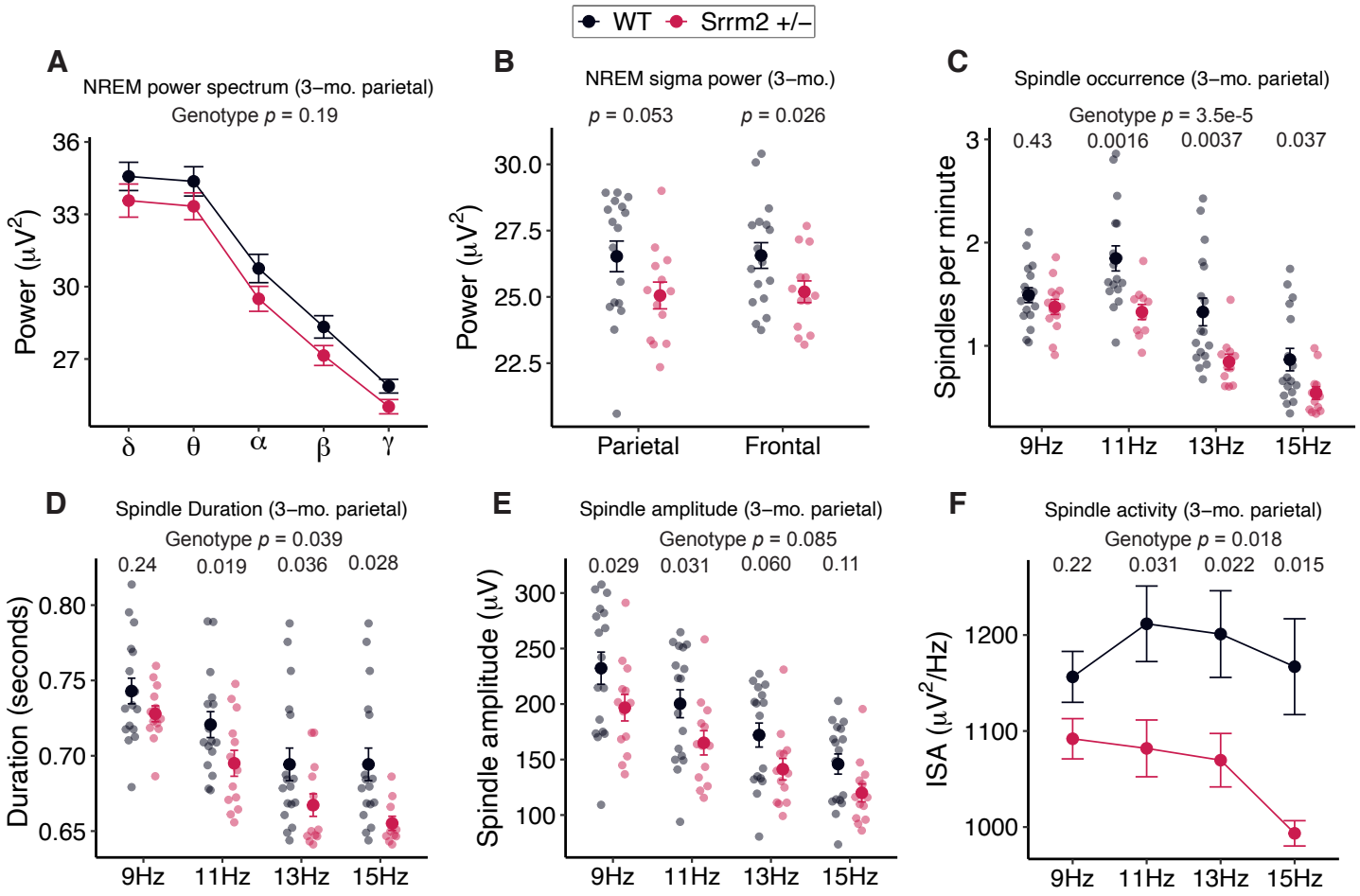
WT
Srrm2 +/–
A
NREM power spectrum (3–mo. parietal)
Genotype p = 0.19
Power (μV²)
36
33
30
27
δ
θ
α
β
γ
B
NREM sigma power (3–mo.)
p = 0.053
p = 0.026
Power (μV²)
30.0
27.5
25.0
22.5
Parietal
Frontal
C
Spindle occurrence (3–mo. parietal)
Genotype p = 3.5e-5
0.43
0.0016
0.0037
0.037
Spindles per minute
3
2
1
9Hz
11Hz
13Hz
15Hz
D
Spindle Duration (3–mo. parietal)
Genotype p = 0.039
0.24
0.019
0.036
0.028
Duration (seconds)
0.80
0.75
0.70
0.65
9Hz
11Hz
13Hz
15Hz
E
Spindle amplitude (3–mo. parietal)
Genotype p = 0.085
0.029
0.031
0.060
0.11
Spindle amplitude (μV)
300
250
200
150
100
9Hz
11Hz
13Hz
15Hz
F
Spindle activity (3–mo. parietal)
Genotype p = 0.018
0.22
0.031
0.022
0.015
ISA (μV²/Hz)
1200
1100
1000
9Hz
11Hz
13Hz
15Hz

Fig. S1

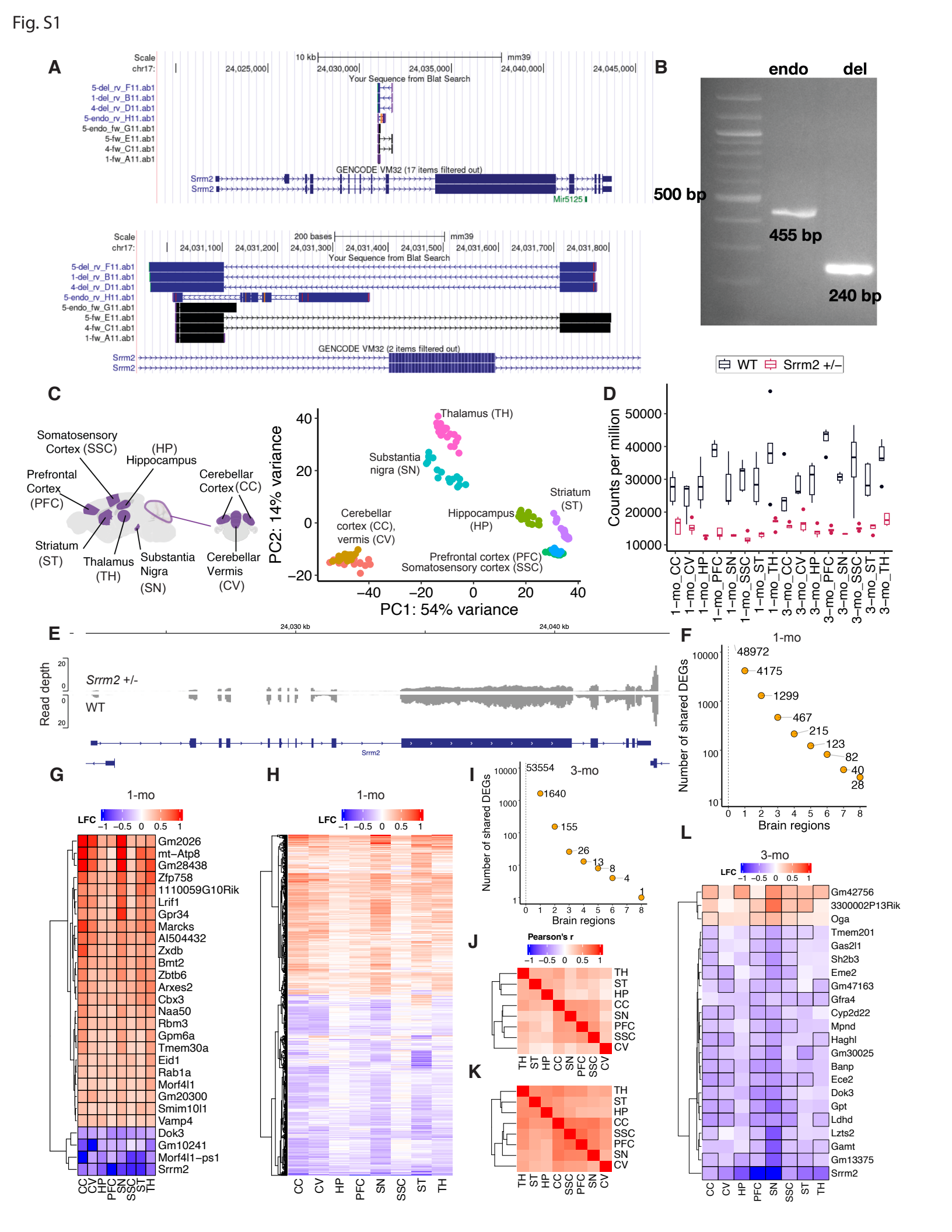
A
Scale
chr17:
10 kb
mm39
24,025,000
24,030,000
24,035,000
24,040,000
24,045,000
Your Sequence from Blat Search
5-del_rv_F11.ab1
1-del_rv_B11.ab1
4-del_rv_D11.ab1
5-endo_rv_H11.ab1
5-endo_fw_G11.ab1
5-fw_E11.ab1
4-fw_C11.ab1
1-fw_A11.ab1
GENCODE VM32 (17 items filtered out)
Srrm2
Srrm2
Mir5125
200 bases
24,031,100
24,031,200
24,031,300
24,031,400
24,031,500
24,031,600
24,031,700
24,031,800
GENCODE VM32 (2 items filtered out)
B
endo
del
500 bp
455 bp
240 bp
WT
Srrm2 +/–
C
Somatosensory Cortex (SSC)
(HP) Hippocampus
Prefrontal Cortex (PFC)
Cerebellar Cortex (CC)
Striatum (ST)
Thalamus (TH)
Substantia Nigra (SN)
Cerebellar Vermis (CV)
PC2: 14% variance
PC1: 54% variance
Thalamus (TH)
Substantia nigra (SN)
Striatum (ST)
Cerebellar cortex (CC), vermis (CV)
Hippocampus (HP)
Prefrontal cortex (PFC)
Somatosensory cortex (SSC)
D
Counts per million
1–mo_CC
1–mo_CV
1–mo_HP
1–mo_PFC
1–mo_SN
1–mo_SSC
1–mo_ST
1–mo_TH
3–mo_CC
3–mo_CV
3–mo_HP
3–mo_PFC
3–mo_SN
3–mo_SSC
3–mo_ST
3–mo_TH
E
24,030 kb
24,040 kb
Read depth
Srrm2 +/-
WT
Srrm2
F
1-mo
Number of shared DEGs
Brain regions
48972
4175
1299
467
215
123
82
40
28
G
1-mo
LFC
Gm2026
mt–Atp8
Gm28438
Zfp758
1110059G10Rik
Lrif1
Gpr34
Marcks
AI504432
Zxdb
Bmt2
Zbtb6
Arxes2
Cbx3
Naa50
Rbm3
Gpm6a
Tmem30a
Eid1
Rab1a
Morf4l1
Gm20300
Smim10l1
Vamp4
Dok3
Gm10241
Morf4l1–ps1
Srrm2
CC
CV
HP
PFC
SN
SSC
ST
TH
H
1-mo
LFC
I
3-mo
Number of shared DEGs
Brain regions
53554
1640
155
26
13
8
4
1
J
Pearson's r
TH
ST
HP
CC
SN
PFC
SSC
CV
K
TH
ST
HP
CC
SSC
PFC
SN
CV
L
3-mo
LFC
Gm42756
3300002P13Rik
Oga
Tmem201
Gas2l1
Sh2b3
Eme2
Gm47163
Gfra4
Cyp2d22
Mpnd
Haghl
Gm30025
Banp
Ece2
Dok3
Gpt
Ldhd
Lzts2
Gamt
Gm13375
Srrm2
CC
CV
HP
PFC
SN
SSC
ST
TH

Fig. S2

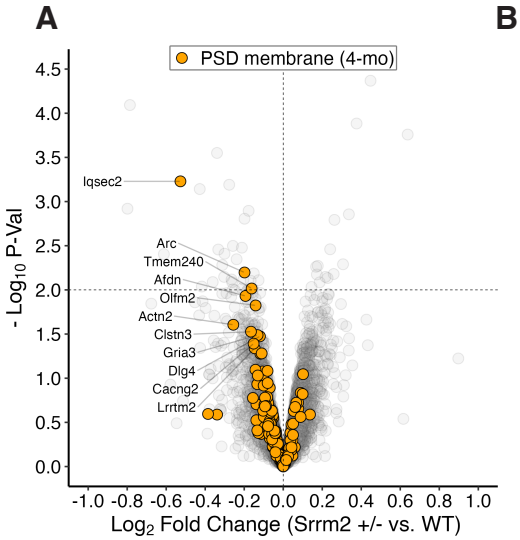
A
PSD membrane (4-mo)
- Log10 P-Val
Log2 Fold Change (Srrm2 +/- vs. WT)
Iqsec2
Arc
Tmem240
Afdn
Olfm2
Actn2
Clstn3
Gria3
Dlg4
Cacng2
Lrrtm2

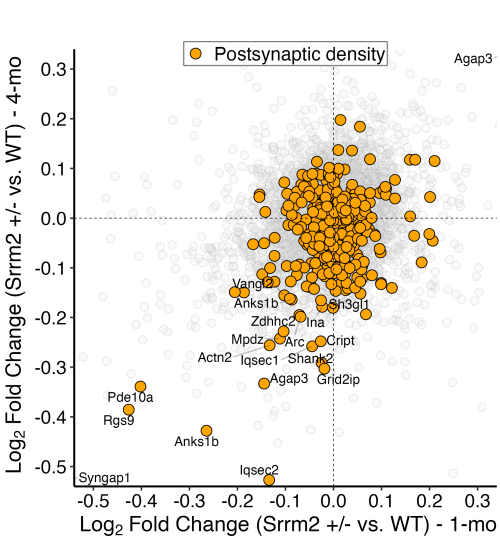
B
Postsynaptic density
Agap3
Log2 Fold Change (Srrm2 +/- vs. WT) - 4-mo
Log2 Fold Change (Srrm2 +/- vs. WT) - 1-mo
Vangl2
Anks1b
Sh3gl1
Zdhhc2
Ina
Mpdz
Arc
Cript
Actn2
Iqsec1
Shank2
Agap3
Grid2ip
Pde10a
Rgs9
Anks1b
Syngap1
Iqsec2

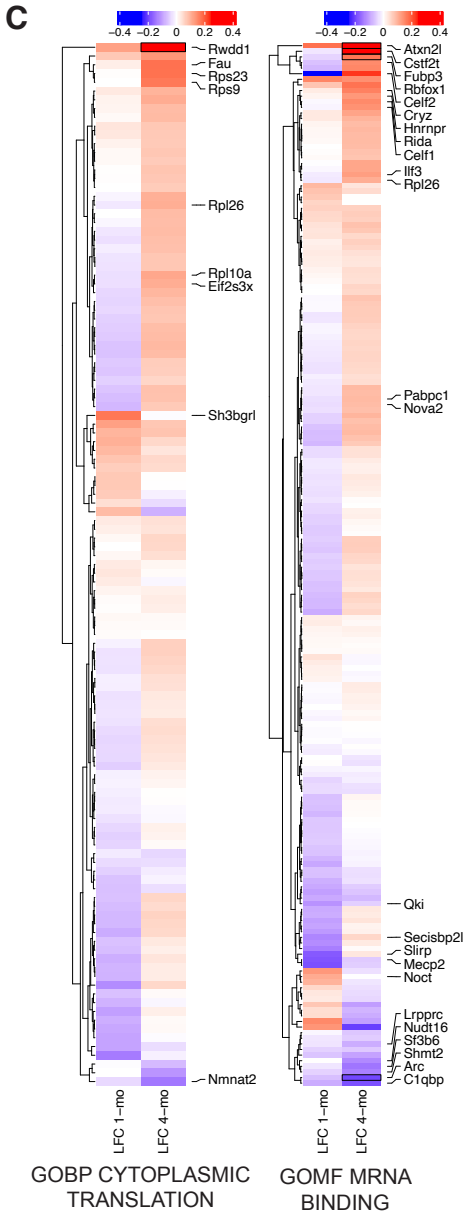
C
Rwdd1
Fau
Rps23
Rps9
Rpl26
Rpl10a
Eif2s3x
Sh3bgrl
Nmnat2
Atxn2l
Cstf2t
Fubp3
Rbfox1
Celf2
Cryz
Hnrnpr
Rida
Celf1
Ilf3
Rpl26
Pabpc1
Nova2
Qki
Secisbp2l
Slirp
Mecp2
Noct
Lrpprc
Nudt16
Sf3b6
Shmt2
Arc
C1qbp
LFC 1−mo
LFC 4−mo
GOBP CYTOPLASMIC TRANSLATION
GOMF MRNA BINDING

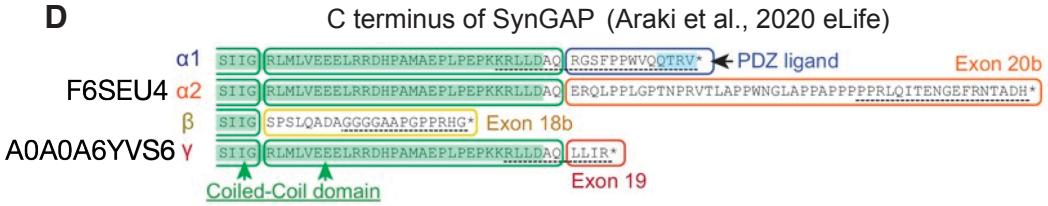
D
C terminus of SynGAP (Araki et al., 2020 eLife)
F6SEU4
A0A0A6YVS6
α1
α2
β
γ
SIIG RLMLVEEELRRDHPAMAEPLPEPKKRLLDAQ RGSFPPWVQQTRV*
PDZ ligand
Exon 20b
ERQLPPLGPTNPRVTLAPPWNGLAPPAPPPPPRLQITENGEFRNTADH*
SPSLQADAGGGGAAPGPPRHG*
Exon 18b
LLIR*
Exon 19
Coiled-Coil domain

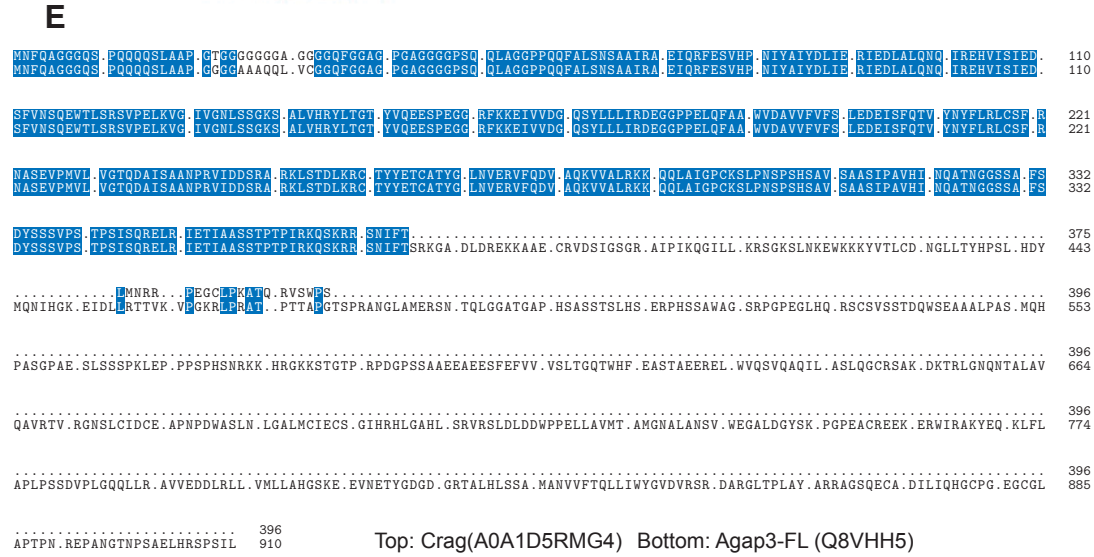
E
Top: Crag(A0A1D5RMG4) Bottom: Agap3-FL (Q8VHH5)

Fig. S3

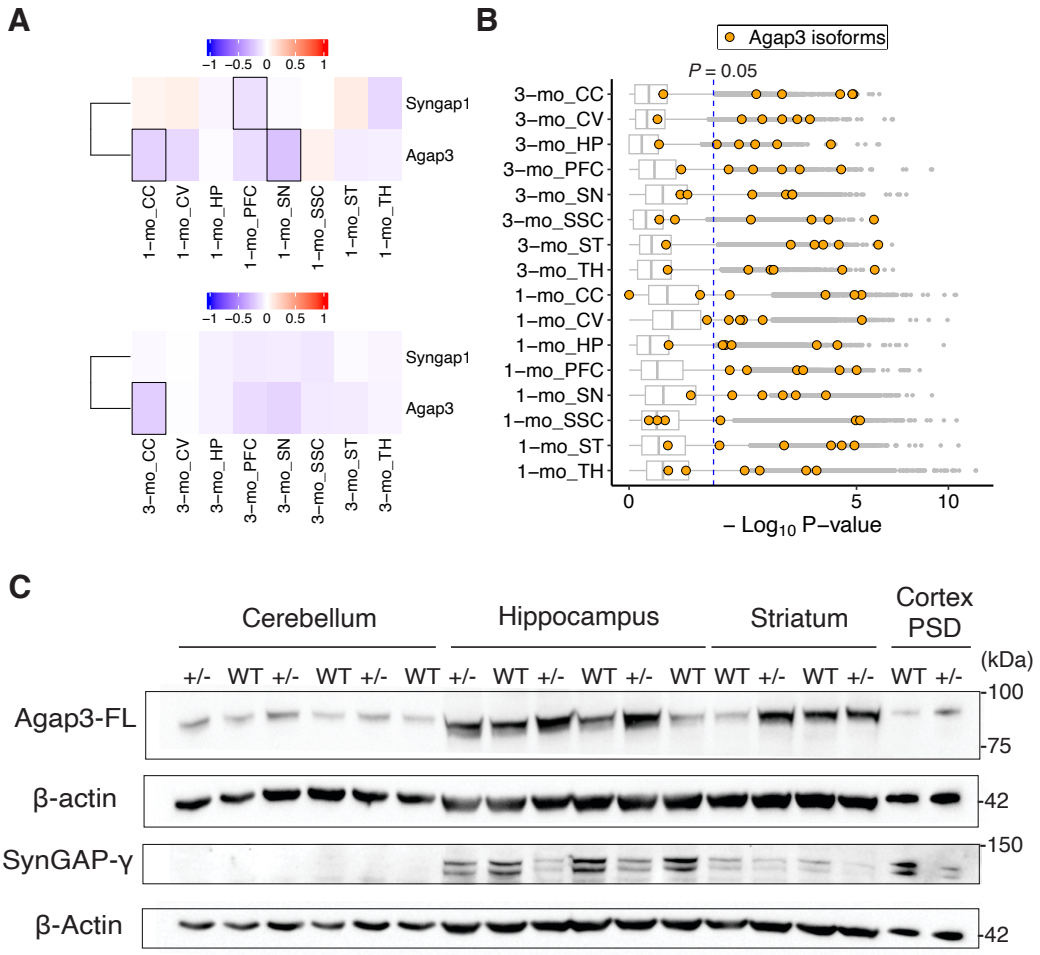
A
−1 −0.5 0 0.5 1
Syngap1
Agap3
1−mo_CC
1−mo_CV
1−mo_HP
1−mo_PFC
1−mo_SN
1−mo_SSC
1−mo_ST
1−mo_TH
3−mo_CC
3−mo_CV
3−mo_HP
3−mo_PFC
3−mo_SN
3−mo_SSC
3−mo_ST
3−mo_TH
B
Agap3 isoforms
P = 0.05
0
5
10
− Log10 P−value
C
Cerebellum
Hippocampus
Striatum
Cortex PSD
+/- WT +/- WT +/- WT +/- WT +/- WT +/- WT WT +/- WT +/- WT +/-
(kDa)
Agap3-FL
β-actin
SynGAP-γ
β-Actin
100
75
42
150
42

Fig. S4

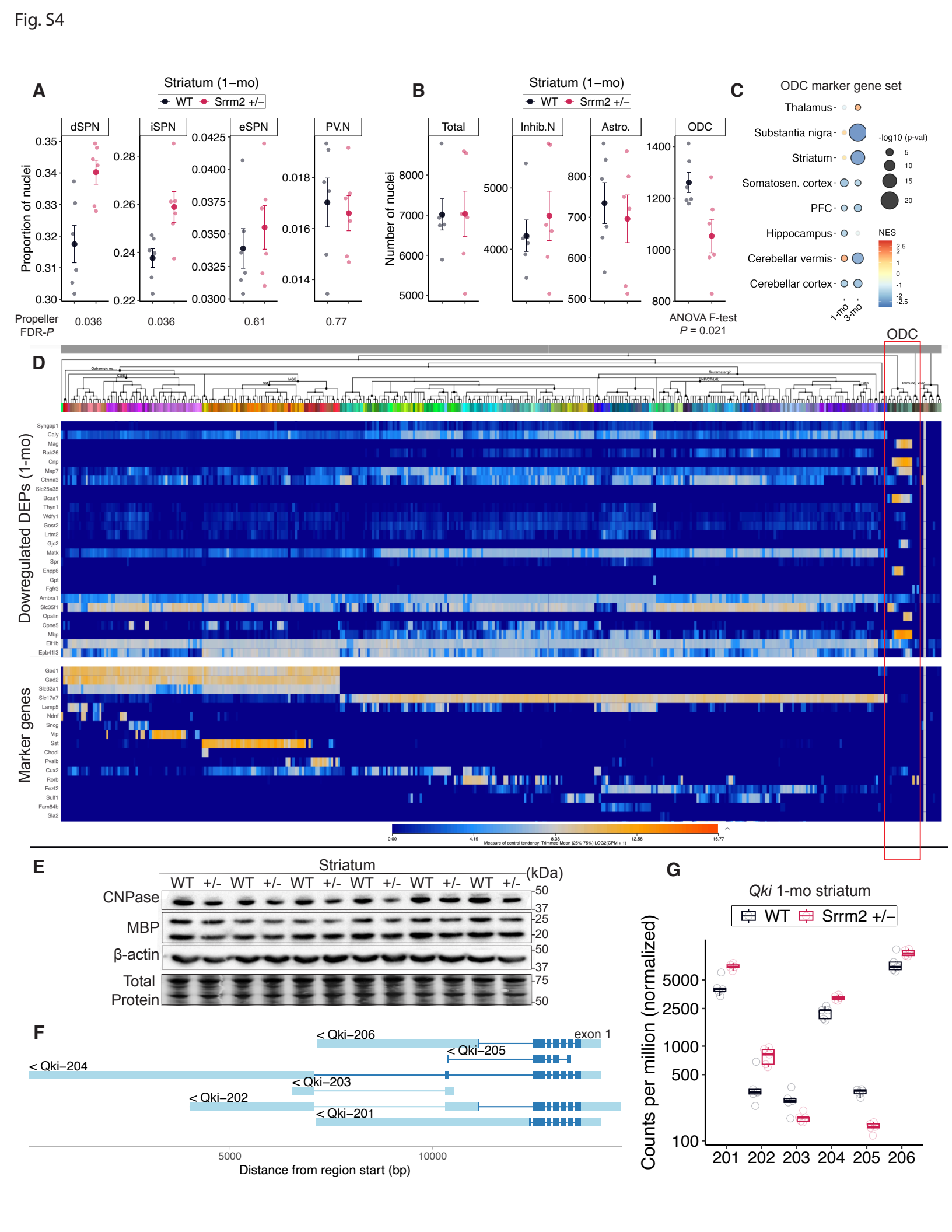
A
Striatum (1–mo)
WT
Srrm2 +/–
dSPN
iSPN
eSPN
PV.N
Proportion of nuclei
Propeller FDR-P
0.036
0.036
0.61
0.77
B
Striatum (1–mo)
WT
Srrm2 +/–
Total
Inhib.N
Astro.
ODC
Number of nuclei
ANOVA F-test
P = 0.021
C
ODC marker gene set
Thalamus
Substantia nigra
Striatum
Somatosen. cortex
PFC
Hippocampus
Cerebellar vermis
Cerebellar cortex
-log10 (p-val)
NES
1-mo
3-mo
D
ODC
Dowregulated DEPs (1-mo)
Syngap1
Caly
Mag
Rab26
Cnp
Map7
Ctnna3
Slc25a35
Bcas1
Thyn1
Wdfy1
Gosr2
Lrtm2
Gjc2
Matk
Spr
Enpp6
Gpt
Fgfr3
Ambra1
Slc35f1
Opalin
Cpne5
Mbp
Eif1b
Epb41l3
Marker genes
Gad1
Gad2
Slc32a1
Slc17a7
Lamp5
Ndnf
Sncg
Vip
Sst
Chodl
Pvalb
Cux2
Rorb
Fezf2
Sulf1
Fam84b
Sla2
Measure of central tendency: Trimmed Mean (25%-75%) LOG2(CPM + 1)
E
Striatum
(kDa)
WT
+/-
CNPase
MBP
β-actin
Total Protein
50
37
25
20
75
F
< Qki–206
exon 1
< Qki–205
< Qki–204
< Qki–203
< Qki–202
< Qki–201
5000
10000
Distance from region start (bp)
G
Qki 1-mo striatum
WT
Srrm2 +/–
Counts per million (normalized)
5000
2500
1000
500
100
201
202
203
204
205
206

Fig. S5

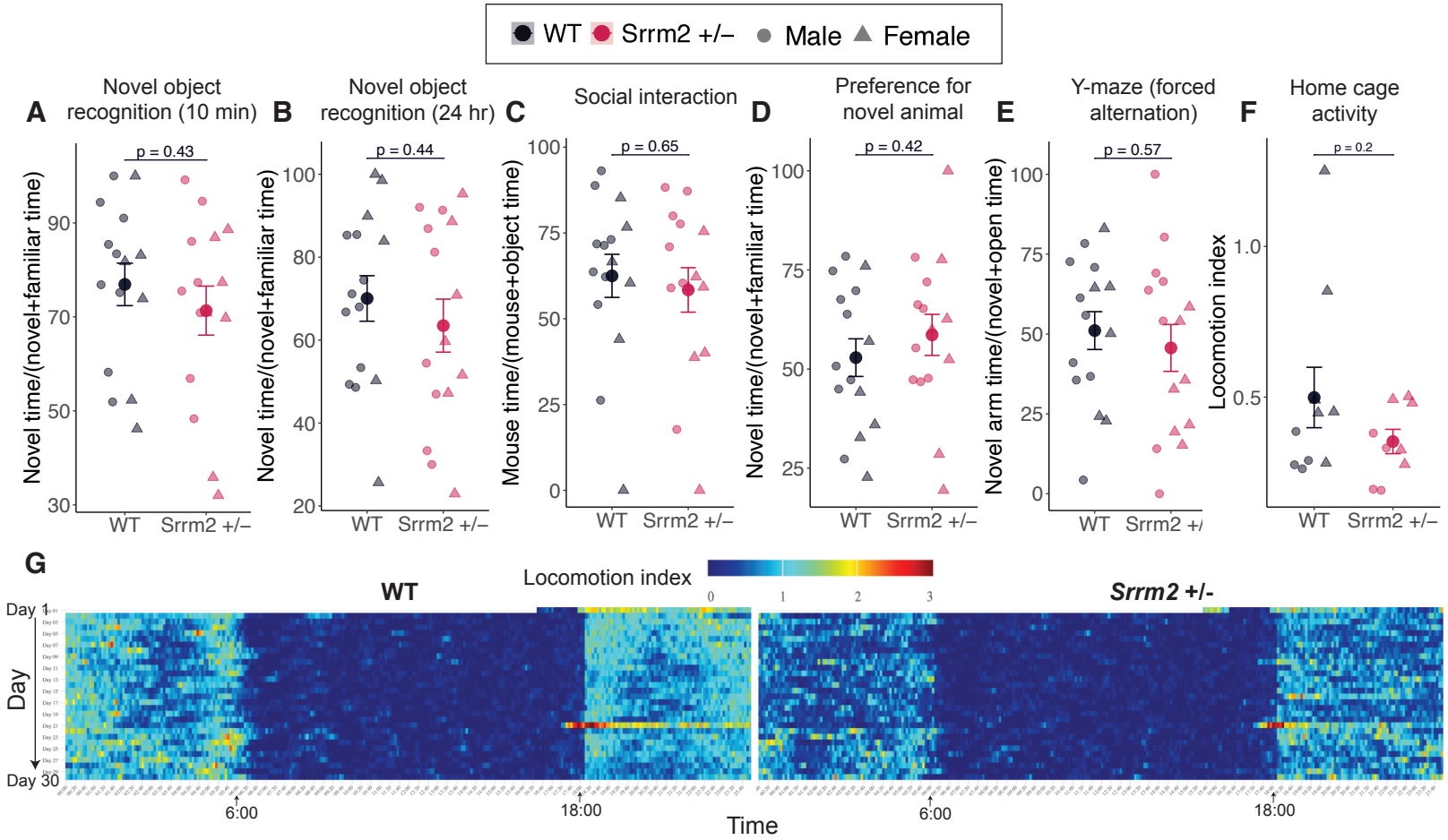
WT
Srrm2 +/–
Male
Female
A
Novel object recognition (10 min)
p = 0.43
Novel time/(novel+familiar time)
WT
Srrm2 +/–
B
Novel object recognition (24 hr)
p = 0.44
Novel time/(novel+familiar time)
C
Social interaction
p = 0.65
Mouse time/(mouse+object time)
D
Preference for novel animal
p = 0.42
Novel time/(novel+familiar time)
E
Y-maze (forced alternation)
p = 0.57
Novel arm time/(novel+open time)
F
Home cage activity
p = 0.2
Locomotion index
G
WT
Locomotion index
Srrm2 +/-
Day 1
Day
Day 30
6:00
18:00
Time

Fig. S6

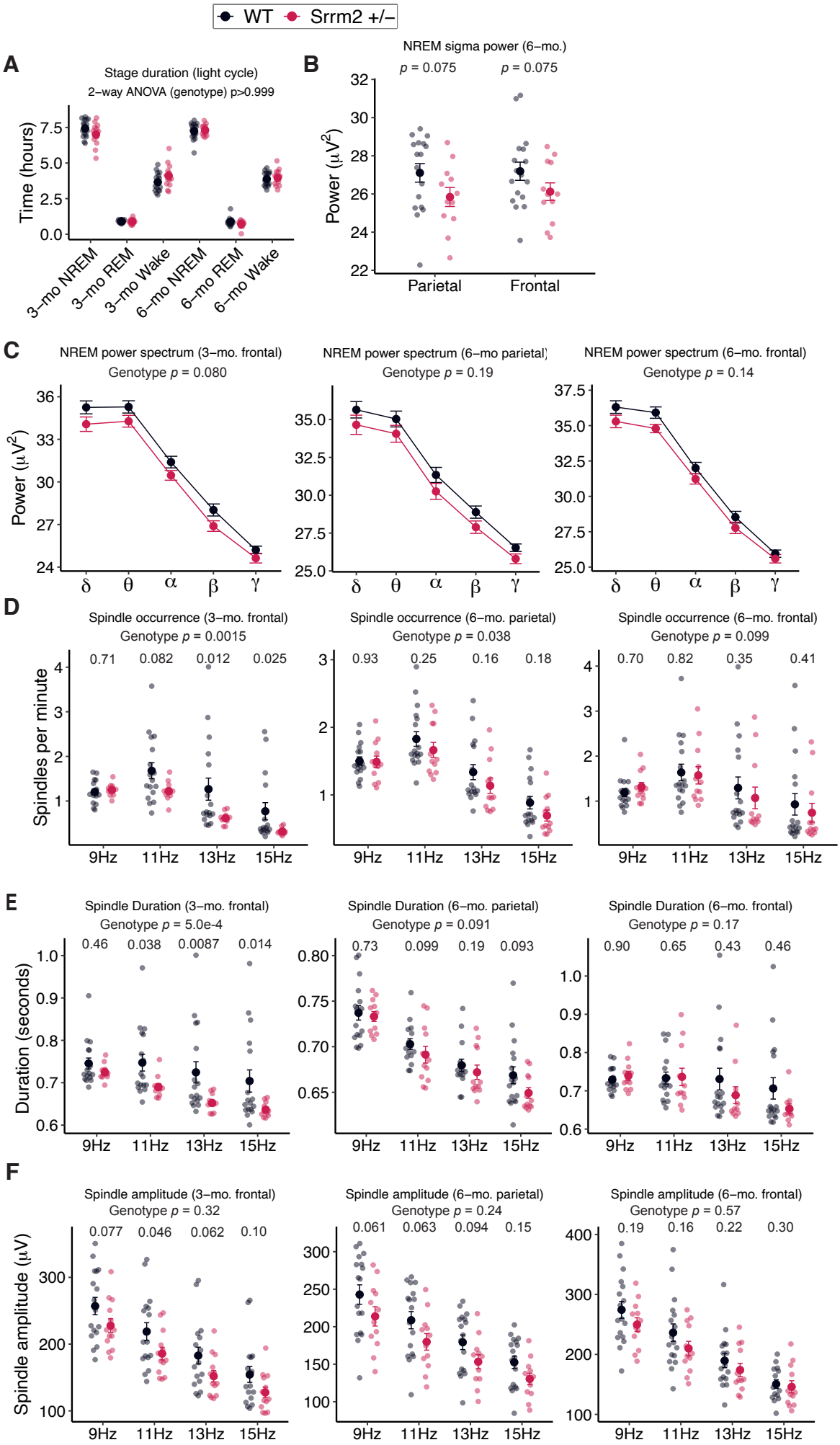
WT
Srrm2 +/–
A
Stage duration (light cycle)
2–way ANOVA (genotype) p>0.999
Time (hours)
3–mo NREM
3–mo REM
3–mo Wake
6–mo NREM
6–mo REM
6–mo Wake
B
NREM sigma power (6–mo.)
p = 0.075
p = 0.075
Power (μV²)
Parietal
Frontal
C
NREM power spectrum (3–mo. frontal)
Genotype p = 0.080
NREM power spectrum (6–mo parietal)
Genotype p = 0.19
NREM power spectrum (6–mo. frontal)
Genotype p = 0.14
Power (μV²)
δ θ α β γ
D
Spindle occurrence (3–mo. frontal)
Genotype p = 0.0015
0.71 0.082 0.012 0.025
Spindle occurrence (6–mo. parietal)
Genotype p = 0.038
0.93 0.25 0.16 0.18
Spindle occurrence (6–mo. frontal)
Genotype p = 0.099
0.70 0.82 0.35 0.41
Spindles per minute
9Hz 11Hz 13Hz 15Hz
E
Spindle Duration (3–mo. frontal)
Genotype p = 5.0e-4
0.46 0.038 0.0087 0.014
Spindle Duration (6–mo. parietal)
Genotype p = 0.091
0.73 0.099 0.19 0.093
Spindle Duration (6–mo. frontal)
Genotype p = 0.17
0.90 0.65 0.43 0.46
Duration (seconds)
9Hz 11Hz 13Hz 15Hz
F
Spindle amplitude (3–mo. frontal)
Genotype p = 0.32
0.077 0.046 0.062 0.10
Spindle amplitude (6–mo. parietal)
Genotype p = 0.24
0.061 0.063 0.094 0.15
Spindle amplitude (6–mo. frontal)
Genotype p = 0.57
0.19 0.16 0.22 0.30
Spindle amplitude (μV)
9Hz 11Hz 13Hz 15Hz